6-8-2022

Identification of Arhgef12 and Prkci as genetic modifiers of retinal dysplasia in the Crb1rd8 mouse model.

Sonia M Weatherly

Gayle B. Collin

Jeremy R. Charette

Lisa Stone

Nattaya Damkham

See next page for additional authors

Authors

Sonia M Weatherly, Gayle B. Collin, Jeremy R. Charette, Lisa Stone, Nattaya Damkham, Lillian F Hyde, James G Peterson, Wanda L. Hicks, Gregory W. Carter, Juergen K. Naggert, Mark P. Krebs, and Patsy M. Nishina

RESEARCH ARTICLE

Identification of *Arhgef12* and *Prkci* as genetic modifiers of retinal dysplasia in the *Crb1^rd8^* mouse model

Sonia M. Weatherly[1], **Gayle B. Collin**[1], **Jeremy R. Charette**[1], **Lisa Stone**[1], **Nattaya Damkham**[1,2,3], **Lillian F. Hyde**[1], **James G. Peterson**[1], **Wanda Hicks**[1], **Gregory W. Carter**[1], **Jürgen K. Naggert**[1], **Mark P. Krebs**[1]*, **Patsy M. Nishina**[1]*

1 The Jackson Laboratory, Bar Harbor, Maine, United States of America, 2 Graduate Program in Immunology, Department of Immunology, Faculty of Medicine Siriraj Hospital, Mahidol University, Bangkok, Thailand, 3 Siriraj Center of Excellence for Stem Cell Research, Faculty of Medicine Siriraj Hospital, Mahidol University, Bangkok, Thailand

* mark.krebs@jax.org (MPK); patsy.nishina@jax.org (PMN)

Abstract

Mutations in the apicobasal polarity gene *CRB1* lead to diverse retinal diseases, such as Leber congenital amaurosis, cone-rod dystrophy, retinitis pigmentosa (with and without Coats-like vasculopathy), foveal retinoschisis, macular dystrophy, and pigmented paravenous chorioretinal atrophy. Limited correlation between disease phenotypes and *CRB1* alleles, and evidence that patients sharing the same alleles often present with different disease features, suggest that genetic modifiers contribute to clinical variation. Similarly, the retinal phenotype of mice bearing the *Crb1* retinal degeneration 8 (*rd8*) allele varies with genetic background. Here, we initiated a sensitized chemical mutagenesis screen in B6.Cg-*Crb1^rd8^*/Pjn, a strain with a mild clinical presentation, to identify genetic modifiers that cause a more severe disease phenotype. Two models from this screen, *Tvrm266* and *Tvrm323*, exhibited increased retinal dysplasia. Genetic mapping with high-throughput exome and candidate-gene sequencing identified causative mutations in *Arhgef12* and *Prkci*, respectively. Epistasis analysis of both strains indicated that the increased dysplastic phenotype required homozygosity of the *Crb1^rd8^* allele. Retinal dysplastic lesions in *Tvrm266* mice were smaller and caused less photoreceptor degeneration than those in *Tvrm323* mice, which developed an early, large diffuse lesion phenotype. At one month of age, Müller glia and microglia mislocalization at dysplastic lesions in both modifier strains was similar to that in B6.Cg-*Crb1^rd8^*/Pjn mice but photoreceptor cell mislocalization was more extensive. External limiting membrane disruption was comparable in *Tvrm266* and B6.Cg-*Crb1^rd8^*/Pjn mice but milder in *Tvrm323* mice. Immunohistological analysis of mice at postnatal day 0 indicated a normal distribution of mitotic cells in *Tvrm266* and *Tvrm323* mice, suggesting normal early development. Aberrant electroretinography responses were observed in both models but functional decline was significant only in *Tvrm323* mice. These results identify *Arhgef12* and *Prkci* as modifier genes that differentially shape *Crb1*-associated retinal disease, which may be relevant to understanding clinical variability and underlying disease mechanisms in humans.

Author summary

Inherited eye diseases affect roughly 1:1,000 individuals worldwide. Although these diseases are often linked to variants of a single gene, it is increasingly recognized that a second variant in other genes may modify disease characteristics, including age of onset, severity, and lesion appearance. Identifying such modifier genes in humans is difficult. In this study, two modifiers of a gene associated with retinal damage leading to childhood blindness in humans (*CRB1*) were identified in mice. Retinal damage caused by *Crb1* mutation alone was less severe than in the presence of *Arhgef12* or *Prkci* mutations. Furthermore, the modifier gene mutations caused retinal damage only in the presence of the *Crb1* mutation. Our results point to a role of mouse *Crb1* and the modifying effects of *Arhgef12* and *Prkci* in a biological network that controls adhesive interactions between cells. The variation in disease severity, lesion appearance, and visual responses in these mice provide a dramatic example of modifier gene influence. This work may lead to an improved understanding of the molecular basis of *CRB1*-associated retinal disease, with possible relevance to diagnostic and therapeutic intervention in humans.

Introduction

Inherited retinal dystrophies associated with variants of the apicobasal polarity gene *CRB1* exhibit a perplexing diversity of disease phenotypes (reviewed in [1–6]), including Leber congenital amaurosis (LCA8, MIM 613835), early-onset rod-cone dystrophy, juvenile- or adult-onset retinitis pigmentosa (RP) with or without paraarteriolar preservation of the retinal pigment epithelium (RP12, MIM 600105), cone-rod dystrophy, RP with Coats-like exudative vasculopathy (retinal telangiectasia), hypermetropia, keratoconus, foveal retinoschisis and cystic or retinoschisis-like maculopathy and macular dystrophy, and pigmented paravenous chorioretinal atrophy (PPCRA, MIM 172870). This variability in disease onset, progression, severity, topography, and specific pathological features makes it difficult to advise patients about therapeutic options and key quality of life issues, and to identify suitable patients for participation in prospective clinical trials [7]. Identifying the genetic and/or environmental factors responsible for clinical variability may therefore refine the prognosis of *CRB1*-associated diseases and promote the development of therapeutic approaches.

Clinical variability may reflect the many biological processes in which CRB1 participates. *CRB1* encodes a mammalian member [8] of a family of transmembrane proteins related to Drosophila Crumbs (Crb) [9], which are central to conserved CRB complexes that govern epithelial apicobasal polarity, cell-cell adhesion, apical segregation of proteins and lipids, cellular size and shape determination, intercellular signaling, cell division, and tissue morphogenesis [4,10–14]. In the Drosophila eye, Crb localizes to the stalk subdomain of the photoreceptor cell apical membrane, where it mediates the assembly of adherens junctions and the apical segregation of cellular components [13,15–17]. Homozygous mutations of crb disrupt photoreceptor cell morphogenesis and cause photoreceptor cell apoptosis and retinal degeneration [16,18]. In the mouse and human retina, CRB1 is most prominently localized to the subapical region of the neural retina, specifically in photoreceptor inner segments above adherens and tight junctions, and in Müller cell apical processes [8,16,19,20]. CRB1 disruption in mice perturbs cell-cell adhesion at the external limiting membrane (ELM), as indicated by the focal loss of adherens junctions [19,21]. CRB1 disruption is also associated with outer retinal folds and pseudorosettes (retinal dysplasia) that correspond to light spots observed by fundus

examination, and with photoreceptor degeneration in dysplastic regions [19–23]. Thus, CRB1 engages in multiple activities affecting cell and tissue integrity, raising the possibility that the variability of *CRB1/Crb1*-associated retinal disease arises from the differential disruption of these activities.

One hypothesis to explain disease variability is that *CRB1* variants have allele-specific effects. Nearly 300 pathogenic or likely pathogenic *CRB1* alleles have been identified (https://databases.lovd.nl/shared/genes/CRB1). Alleles may differ in their effect on protein levels, stability, or function, and variants affecting specific protein domains might be associated with distinct *CRB1*-disease subtypes. Although most efforts to establish genotype-phenotype correlations have met with limited success to date [1–6], some recent clinical studies indicate potential correlations [7,24,25]. The correlation of disease-causing missense substitutions in the extracellular domains of Drosophila Crb with variable cellular and retinal degeneration phenotypes [26] and the recent identification of a novel photoreceptor-specific isoform, CRB1-B, in human and mouse retinas [21], may provide new perspectives for understanding these allele-specific effects.

It has also been suggested that variation in modifier genes may contribute to *CRB1*-associated disease variability. For example, mutations in genes encoding proteins that may directly or indirectly interact with *CRB1* could potentially mediate different pathogenic effects. In support of this hypothesis, distinct and variable disease phenotypes have been observed among individuals with identical *CRB1* alleles, suggesting the existence of genetic modifiers [2–4,6,7,27–29]. Additionally, in about 30% of affected individuals only a single *CRB1* variant allele has been detected suggesting that other genetic variants, possibly including modifier loci, may contribute to the disease [2]. However, apart from a report that an allele of the LCA and RP gene, *AIPL1*, acted as a potential modifier of *CRB1* retinal pathology [30], modifiers in the human population have not been identified. Identification and validation of modifier genes is challenging given the limited number of affected individuals for rare diseases, such as those associated with *CRB1* variants, the genetic heterogeneity of the human population, and the possible effects of undefined environmental factors on disease phenotype.

The successful use of mouse models to identify genetic modifiers of human diseases [31,32] extends to models of eye diseases [33], including *CRB1*-associated retinal dystrophy. Early evidence for genetic modifiers in a *CRB1*-disease model was obtained from studies of STOCK *Crb1*^{rd8}. This genetically mixed inbred strain exhibited extensive dysplasia observed as light spots in the inferior nasal retina by indirect ophthalmoscopy and fundus imaging, which correspond to outer retinal pseudorosettes and folds [19,34]. In segregating crosses of STOCK *Crb1*^{rd8} with the wild-type strains CAST/EiJ or C57BL/6J (B6), the dysplastic phenotype was suppressed [19,34], indicating an effect of genetic background. Independent evidence for modifiers of the phenotype was obtained from breeding studies of strains harboring *Crb1*^{rd8} [35]. Variability of the dysplastic phenotype was also noted among mice derived from the C57BL/6N (B6N) substrain, which is homozygous for the *Crb1*^{rd8} allele [36], and in strains from The Jackson Laboratory (JAX) collection [37]. *Cx3cr1*, *Mthfr*, and *Cygb* were identified as modifiers of *Crb1*^{rd8} retinal dysplasia [38–40], *Jak3* as an enhancer of a *Crb1*^{rd8}-dependent neovascular phenotype [41], and *Crb2* as a modifier of retinal dysplasia due to a *Crb1* knock-out allele [42,43]. Further, the choroidal neovascularization phenotype of an *Nfe2l2* knock-out strain [44] was more severe in the presence of homozygous *Crb1*^{rd8} alleles [45], indicating gene interaction. These studies reveal substantial variability in the retinal phenotype of *Crb1* mutant mice depending on genetic background and demonstrate that modifier genes can be identified. However, the modifiers identified so far do not appear to participate in shared pathways, so identification of additional modifier genes is needed to reveal the cellular and molecular networks that account for all of the observed *CRB1*-disease variability.

Here, as part of the Translational Vision Research Models (TVRM) program [46–48], we identified genetic modifiers that cause a more severe *Crb1rd8* dysplastic retinal phenotype using a sensitized *N*-ethyl-*N*-nitrosourea (ENU) mutagenesis screen of B6.Cg-*Crb1rd8*/Pjn (hereafter B6 *rd8*) mice. These mice are congenic on the B6 background, homozygous for the *Crb1rd8* allele, and exhibit a near-normal fundus appearance [19]. Two mutant modifier lines, *Tvrm266* and *Tvrm323*, were found, respectively, to carry mutations in *Arhgef12*, which encodes guanine nucleotide exchange factor 12, a modulator of Rho GTPase activity, and *Prkci*, which encodes a protein homologous to Drosophila atypical protein kinase C, a component of the Baz-aPKC-Par-6 polarity complex that engages with Crb [10,49]. This work extends the network of apicobasal polarity components that influence *CRB1*-associated retinal disease and underscores its complexity and interconnectivity with multiple molecules and pathways.

Results

Sensitized chemical mutagenesis screen of *Crb1rd8* mice

Identification of variants contributing to the severe dysplastic phenotype in STOCK *Crb1rd8* mice by classic genetical means of recombinant mapping proved to be inconclusive, likely due to multigenic effects and gene interactions. Therefore, to identify genetic modifiers of *Crb1rd8* dysplasia, two sensitized mutagenesis screens were considered initially: mutagenesis of STOCK *Crb1rd8* mice and screen for decreased severity of the fundus spotting phenotype, or mutagenesis of B6 *rd8*, an incipient congenic strain with a mild phenotype [19], and screen for increased severity of the phenotype. Mutagenesis of STOCK *Crb1rd8* males failed to yield pups in repeated attempts with varying concentrations and timing of ENU injections. Thus, mutagenized B6 *rd8* males were bred according to an established strategy to detect both dominant and recessive mutations [46], and the resulting G_3 population screened for an increased spotting phenotype (Fig 1).

Identification of mutations

Two mutant lines, *Tvrm266* and *Tvrm323*, exhibited a heritable, bilateral increase in fundus spots in the inferior nasal retina compared to the parental B6 *rd8* mice (Fig 2A) and were backcrossed for a minimum of five generations to unmutagenized B6 *rd8* to remove unlinked mutations prior to characterization. A high fraction of affected progeny during initial intercrosses to expand the colony suggested that the phenotype in both strains might be semi-dominant. The modifier loci were mapped by crossing these strains with B6N mice, which are homozygous for the *Crb1rd8* allele [36] and have diverged sufficiently from B6 to allow for chromosomal mapping of the modifying loci without contributing to the observed disease phenotypes. For *Tvrm266* mice, high-throughput whole-exome sequencing of affected individuals was first performed to identify likely mutation candidates. For *Tvrm323* mice, a genome-wide recombinational mapping screen (S1 Fig and S1 Data) of 103 backcross progeny ((*Tvrm323* × B6N) F_1 × B6N) revealed that the interval yielding the highest frequency of affected heterozygotes (72%) was a 15.3 Mbp region of Chromosome 3 (Chr 3; 03–021837059 to 03–037129353). Putative causative mutations were identified in *Arhgef12*, by Sanger sequencing confirmation of candidate gene variants detected from the whole-exome sequences of *Tvrm266* mice, and in *Prkci*, by candidate gene sequencing within the confidence interval identified by mapping *Tvrm323* mice (Figs 2B and S2). T to A point mutations occurred in both models resulting in an early stop signal at codon 24 of *Arhgef12* (Fig 2B, *asterisk*) and substitution of asparagine for tyrosine at codon 136 of *Prkci*. Co-segregation of disease phenotype with the mutations identified was statistically significant by endpoint genotyping analysis of 16
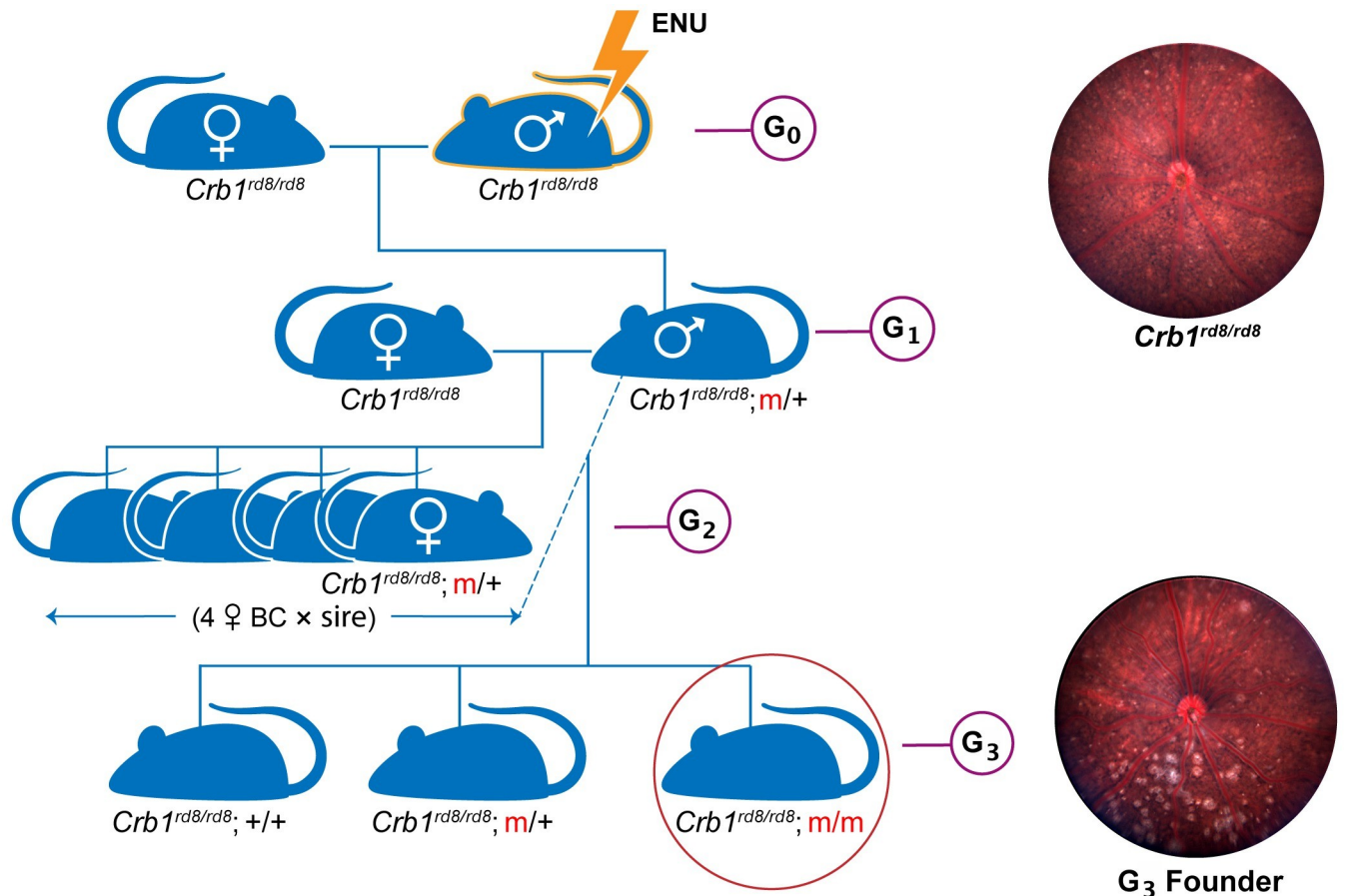
Fig 1. Breeding strategy for chemical mutagenesis. B6 *rd8* G_0 males were treated with N-ethyl-N-nitrosourea (ENU). After about three months when G_0 males regained fertility, they were mated to B6 *rd8* females to produce G_1 progeny. G_1 males were mated to produce G_2 progeny, of which four females were backcrossed with the same G_1 male to produce G_3 progeny. G_3 mice were screened by indirect ophthalmoscopy for evidence of increased retinal dysplasia. G_3 founders were developed into TVRM models by testing for heritability and further backcrossing to remove unlinked mutagenized genes. The increased spotting phenotype typical of retinal dysplasia is evident by comparing the fundus images of a B6 *rd8* mouse (G_0) and a G_3 founder at 12 weeks of age. Homozygosity of the *Crb1^rd8* allele is designated as *rd8/rd8*; mutant alleles of candidate modifier loci are designated as m/+ (heterozygous) or m/m (homozygous).

https://doi.org/10.1371/journal.pgen.1009798.g001

progeny from a *Tvrm266* mapping cross (*Tvrm266* × B6N) F_1 × B6N; $p = 0.010$, Fisher's Exact Test) and by sequencing 12 progeny from the *Tvrm323* mapping cross ($p = 5.4 \times 10^{-5}$, Fisher's Exact Test), indicating that these mutations are causative (S2 Fig).

To assess the effect of the mutations on expression of the encoded proteins, western analysis was performed on posterior eyecups. Analysis of ARHGEF12 in control B6 (Figs 2C and S3) and B6 *rd8* (S3 Fig) samples revealed a single band near the predicted molecular weight of ARHGEF12 (171 kDa predicted for isoform X1, XP_017169054.1). Similar analysis of PRKCI in B6 mice revealed a 66,000 M_r band consistent with the 65 kDa predicted for isoform X1 (XP_006535474). Quantitative western analysis (S4 Fig and S1 Data) indicated that the level of ARHGEF12 in *Tvrm266* eyes was no more than 0.037 of that in B6 eyecups (Student's t-test, $p = 0.0015$); this value is likely to be an overestimate arising from non-specific staining of other eyecup proteins in the blot region analyzed. Little to no expression is expected due to the premature stop codon caused by the mutation. The expression of ARHGEF12 in both B6 and B6 *rd8* mice (S3 Fig) suggested that the homozygous *Crb1* mutation was not the cause of the dramatic decrease in ARHGEF12 expression in *Tvrm266* mice. PRKCI levels in *Tvrm323* mice
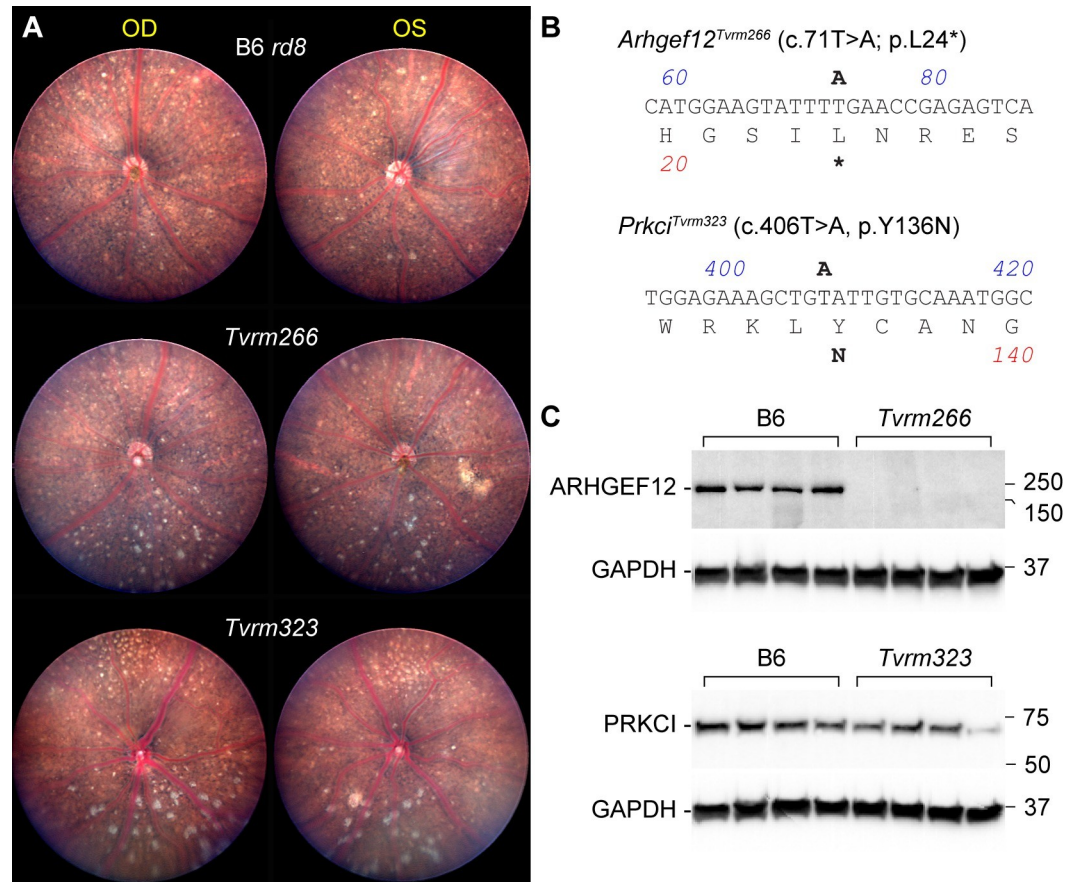
Fig 2. Identification of mutations and protein expression in modifier strains. A. Fundus photodocumentation of B6 *rd8* and *Tvrm266* mice at 10 weeks of age, and *Tvrm323* mice at 3 months of age. Right (OD) and left (OS) eyes of a single mouse are shown. The lower portion of each image corresponds to the inferior retina based on the position of the mouse head relative to the camera during imaging. B. Sequence and amino acid translation of the mutant alleles. The DNA sequence corresponds to a portion of the forward strand of each gene, numbered as in the mRNA. Mutations are indicated in *bold* above the sequence. The predicted amino acid sequence is given beneath the DNA sequence using the single-letter code and the predicted translational effect of the mutation is indicated in *bold* below. C. Enhanced chemiluminescence western analysis. Posterior eyecup lysates from B6 control and modifier strains (n = 4) were electrophoresed and transferred to nitrocellulose. *Tvrm266* blots were probed with ARHGEF12 antibody and *Tvrm323* blots with PRKCI antibody. After imaging, blots were probed with GAPDH antibody and reimaged to control for protein recovery and loading. Molecular weights of protein standards are indicated in kDa.

were 0.57 of those in B6 mice but this effect was not statistically significant (Student's t-test, $p = 0.052$). Comparison of B6 *rd8*, *Tvrm266*, and *Tvrm323* to B6 control eyecups by qRT-PCR (S1 Data) indicated statistically significant differences in *Arhgef12* mRNA levels among strains (one-way ANOVA of ΔC_t values, $F[3,20] = 6.869$, $p = 0.0023$). Dunnet's *post-hoc* test revealed a significant decrease in *Arhgef12* mRNA levels (0.74 of B6, $p = 0.0018$) but not in other strains. This decrease may reflect nonsense-mediated decay of a subset of *Arhgef12* transcripts in *Tvrm266* mice. Parallel analysis of *Prkci* mRNA did not indicate significant *post hoc* differences among the strains compared to B6 controls (S1 Data). Taken together, these results establish novel alleles of two genes as candidate modifiers of the *Crb1^{rd8}* fundus phenotype. The full designation for these models is B6.Cg-*Crb1^{rd8}* *Arhgef12^{Tvrm266}*/Pjn and B6.Cg-*Crb1^{rd8}* *Prkci^{Tvrm323}*/Pjn; for simplicity, we retain the original strain designations *Tvrm266* and *Tvrm323*, respectively, for the remainder of the paper, and unless otherwise indicated the genotype is homozygous for both *Crb1^{rd8}* and the modifier.

Epistasis of *Crb1*^{rd8} modifier genes

We postulated that the increased retinal spotting phenotypes of *Tvrm266* and *Tvrm323* may be due to the new mutations acting alone or through an interaction with *Crb1*^{rd8}. To distinguish these possibilities, we tested for epistasis, classically defined as the masking of a phenotype associated with a variant at one locus by a variant at a second [50]. To examine epistatic interactions, each modifier strain was outcrossed to B6 mice, which are wild-type for *Crb1*, and F_1 progeny subsequently intercrossed to yield F_2 mice. In the case of *Tvrm266*, F_2 mice progeny were genotyped and intercrossed to produce F_3 mice of select genotypes for additional analysis. An increase in fundus spotting was observed in heterozygous or homozygous *Arhgef12*^{Tvrm266} or *Prkci*^{Tvrm323} mice in the presence of the homozygous, but not heterozygous *Crb1*^{rd8} allele (Fig 3A). The fundus phenotype was more severe in the presence of two alleles (homozygous) than with one allele (heterozygous) of either *Arhgef12*^{Tvrm266} or *Prkci*^{Tvrm323}. These results were extended by indirect ophthalmoscopy to all nine genotypes expected from the epistasis intercross (Fig 3B and 3C). Phenotypes of heterozygous *Crb1*^{rd8} mice were similar to those of B6 mice, which rarely exhibited spots (Fig 3A). Interaction modeling of indirect ophthalmoscopy data (S1 Data) from epistasis crosses of both mutants indicated a significantly improved fit using a model that accounted for gene-gene interaction (Fig 3B and 3C) compared to one that was purely additive (adjusted R^2 value for interacting vs. additive models: *Tvrm266* cross, 0.78 vs. 0.62; *Tvrm323* cross, 0.89 vs. 0.69). An F-ratio test of the F-statistic derived from the two statistical models was significant, indicating superior performance of the interacting model for both mutants (F-statistic and *p* values: *Tvrm266* cross, 26.1 and $p = 6.3 \times 10^{-16}$; *Tvrm323* cross, 97.9 and $p = 5.4 \times 10^{-46}$). Both analyses revealed a significant effect of the heterozygous allele on the phenotype (*Tvrm266* cross, $p = 1.9 \times 10^{-5}$; *Tvrm323* cross, $p = 1.6 \times 10^{-8}$), which was smaller than that of the homozygous allele, confirming the semi-dominant mode of inheritance. Taken together, these results reveal a semi-dominant epistatic interaction between *Arhgef12* or *Prkci* mutant alleles and the *Crb1*^{rd8} mutation leading to increased fundus spotting.

Pathological features of modifier strains

Having established that the *Arhgef12* and *Prkci* alleles modify the *Crb1*^{rd8} phenotype, we sought to gain insights into disease pathogenesis by studying the modified strains. Analysis was performed on homozygous *Tvrm266* and *Tvrm323* mice, as the phenotype could be observed at one month of age. To determine whether increased fundus spotting was correlated with dysplastic lesions and other pathological changes, eyes collected from B6, B6 *rd8*, *Tvrm266*, and *Tvrm323* mice were examined histologically (Fig 4). We defined dysplastic lesions as retinal folds or perturbations resulting in the displacement of photoreceptor nuclei by more than three nuclear diameters from either boundary of the outer nuclear layer (ONL). B6 *rd8* retinas (Fig 4B) were morphologically similar to B6 retinas (Fig 4A) except for rare dysplastic lesions in the inferior retina (Fig 4B, *asterisk*; also compare the higher magnification images in Fig 4E and 4F). By contrast, retinal morphology in the inferior retina was disrupted more extensively in the modifier strains, as reported previously in STOCK *Crb1*^{rd8} mice [19,23,34] and other *Crb1* mutant models [20]. Lesions were also evident in the superior retina of *Tvrm266* and *Tvrm323* mice near the optic nerve head. Dysplastic lesions were larger than those in B6 *rd8* mice (compare Fig 4G and 4H with Fig 4F) and differed between the two modifier strains. In *Tvrm266* mice, the largest lesions (Fig 4C, *asterisks*; Fig 4G) extended toward the inner nuclear layer (INL) and resembled the pseudorosettes described in STOCK *Crb1*^{rd8} mice and other models [19,20,23,34]. By contrast, *Tvrm323* lesions were characterized by displacement of retinal cell layers toward the RPE (Fig 4D, *asterisks*; Fig 4H) and often contained
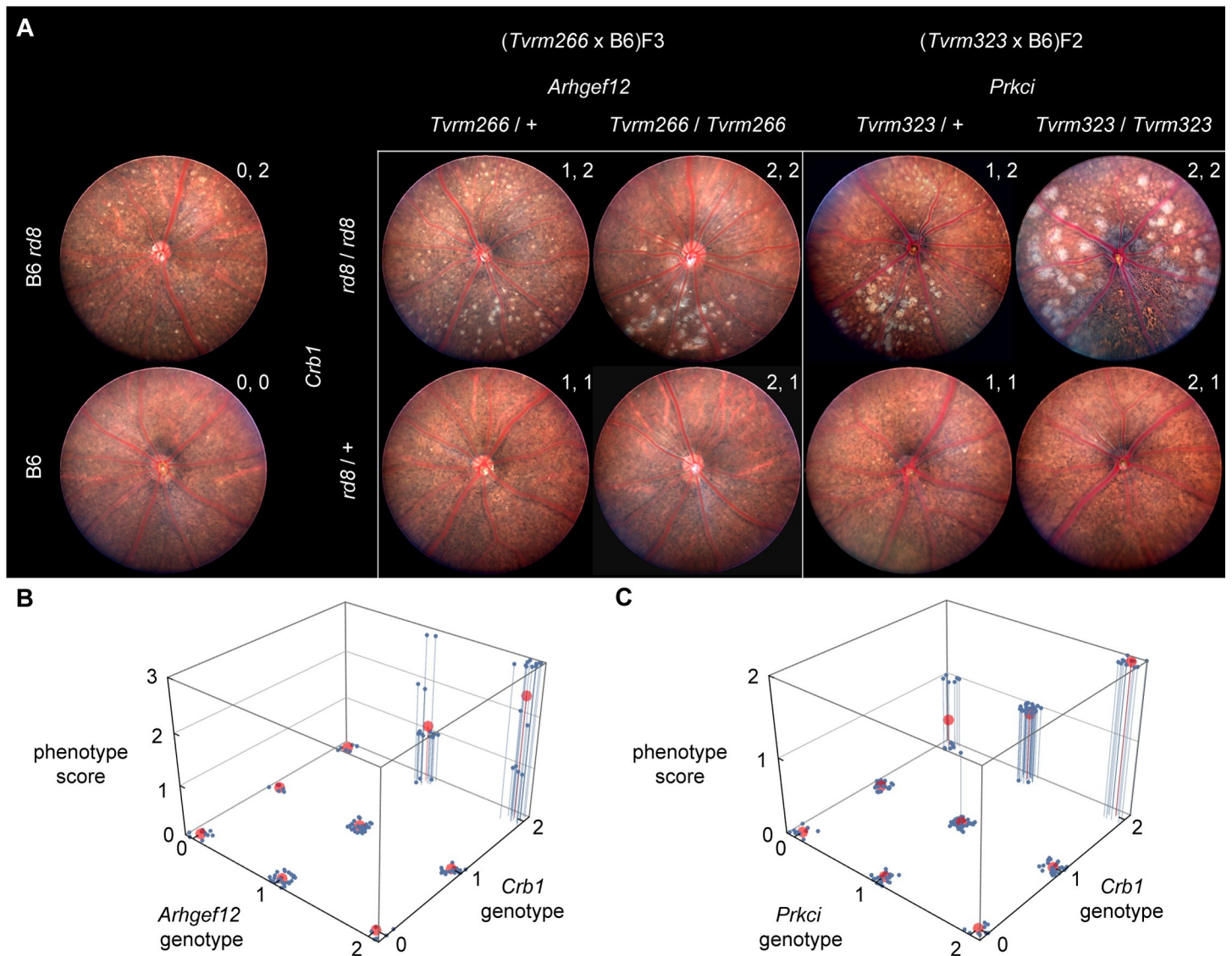
Fig 3. A. Fundus photographs of B6, B6 *rd8*, and F₃ progeny from the *Tvrm266* epistasis cross at 10 weeks of age or F₂ progeny from the *Tvrm323* epistasis cross at 2.5–3.7 months of age. Genotypes are indicated by m/+ (heterozygous) or m/m (homozygous), where m is the mutant allele symbol and, for comparison with panels B and C, by the values a, b at the upper right of each fundus image, which indicate the number of mutant alleles at the modifier and *Crb1* loci, respectively (0, wild-type; 1, heterozygous; 2, homozygous). At least 3 females and 3 males of each genotype were imaged bilaterally. B. 3D plot of the indirect ophthalmoscopy phenotypes of F₂ and F₃ progeny from the *Tvrm266* epistasis cross (9–15 weeks of age) against the nine genotypes expected (n = 6–21 for each genotype). C. Corresponding plot of F₂ phenotypes from the *Tvrm323* epistasis cross (2.5–3.7 months of age; n = 10–48 for each genotype). Indirect ophthalmoscopy annotations were converted to ordinal phenotype scores. Scores for individual mice of each genotype examined are shown in *blue*, with fit statistical models represented by *red circles*. Genotypes values are indicated as in panel A.

https://doi.org/10.1371/journal.pgen.1009798.g003

tubular structures that reached and perturbed cells of this layer (Fig 4H, *red arrowhead*). These structures may represent retinal neovessels, a frequently reported attribute of *Crb1* mutant mice and rats [35,41,51]. A novel feature discovered in modifier strains at one month of age was the presence of apparent voids in the ONL near dysplastic lesions (Fig 4G and 4H, *yellow arrowheads*). One sample with ONL voids was also observed among nine B6 *rd8* mice examined (Fig 4I).

To assess the statistical significance of these findings, histological sections from each independent sample were reviewed for each pathological feature, scoring as affected any samples in
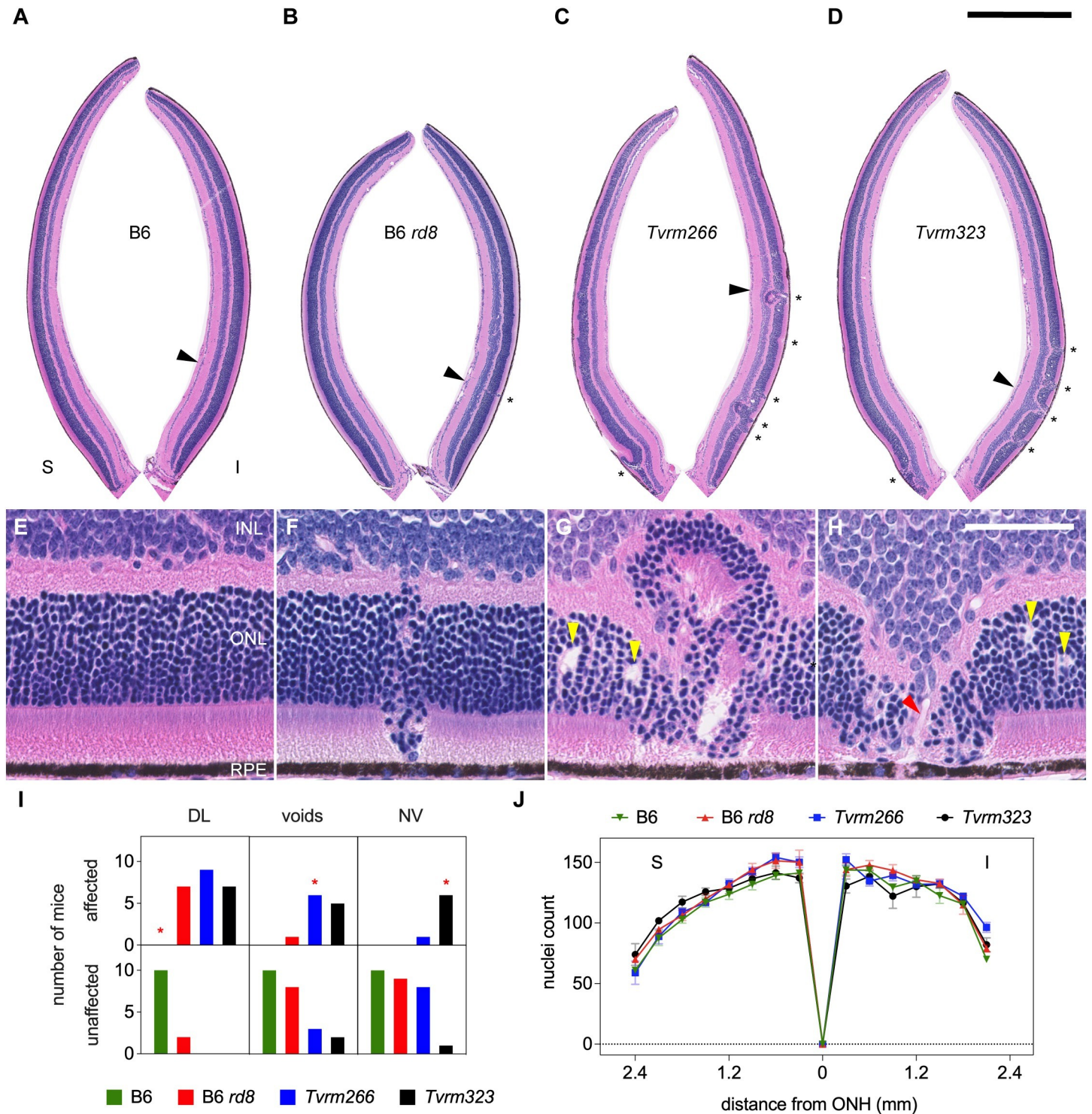
Fig 4. Histological analysis at one month of age. A–D. Superior (S) and inferior (I) retinas cropped from digital images of B6, B6 *rd8*, *Tvrm266* and *Tvrm323* whole eye sections stained with hematoxylin and eosin and imaged with a slide scanner. Dysplastic lesions, *asterisks*. Scale bar, 0.5 mm. Sites from A-D detailed in panels E–H, respectively, are marked by *arrowheads*. E. Normal retinal layers in B6 mice. INL, inner nuclear layer; ONL, outer nuclear layer; RPE, retinal pigment epithelium. F–H. Dysplastic lesions in B6 *rd8*, *Tvrm266*, and *Tvrm323* mice, respectively. Voids in panels G and H, *yellow arrowheads*. H. Lesion containing possible vascular structure, *red arrowhead*. Scale bar, 50 μm; applies to E–H. I. Incidence of pathological features. Mice showing one or more of the identified features among 17–21 reviewed histological sections were scored as affected. *Asterisks* denote statistical significance (Fisher's exact test against B6 *rd8* mice, $p < 0.05$). DL, dysplastic lesions; NV, neovessels. J. Photoreceptor nuclei count within a 50 μm length of retina as a function of distance from the ONH. Values represent mean ± standard error of the mean (SEM); n = 5–8.

https://doi.org/10.1371/journal.pgen.1009798.g004

which the feature occurred at least once. Compared to B6 *rd8* mice, significant differences in incidence were observed only for dysplastic lesions among B6 mice (Fisher's exact test, Bonferroni *post hoc* correction, $p = 0.0021$), and for neovascular lesions among *Tvrm323* mice (Fisher's exact test, Bonferroni *post hoc* correction, $p = 0.0026$; Fig 4I, *asterisks*; S1 Data). To determine whether these pathological changes were associated with photoreceptor degeneration, photoreceptor nuclei were counted in regions corresponding to a fixed length of the retinal perimeter, which were positioned at regular intervals over the entire retina. At one month of age, no significant effect of strain on the number of photoreceptor nuclei was observed among B6 mice or modifier strains compared to B6 *rd8* mice (Fig 4J, repeated measures mixed-effects model, $F_{(3, 22)} = 1.8$, $p = 0.18$; S1 Data). These results show that retinal dysplasia and associated pathological changes occur at an early age prior to significant degeneration. The topographical distribution of lesions in the inferior retina and the superior retina near the ONH matched that of fundus spots, indicating that retinal dysplasia accounts for the increased fundus spotting phenotype.

Age-dependent pathological changes in modifier strains

Most forms of *CRB1* retinal disease are progressive in humans [1–6]. To examine whether progressive changes occurred with age in the modifier strains, histological analysis was repeated at 12 months of age (Fig 5). B6 *rd8* retinal morphology was similar to that of B6 retinas in aged mice (Fig 5A and 5E), except for rare dysplastic lesions as observed at one month of age (Fig 5B and 5F). By contrast, in addition to a continued presence of dysplastic lesions at 12 months of age (Fig 5C and 5D, *asterisks*), retinas in both modifier strains exhibited areas of complete photoreceptor loss, which were more extensive in *Tvrm323* than in *Tvrm266* mice (Fig 5C and 5D, *solid lines*). ONL voids were not observed, but neovascular lesions resulting in RPE perturbation were apparent in both modifier strains at this age (Fig 5G and 5H, *red* and *white arrowheads*). The incidence of neovascular lesions was statistically significant in both modifier strains compared to B6 *rd8* (Fig 5I and S1 Data). Analysis of photoreceptor nuclei counts indicated a statistically significant effect of strain (mixed-effects model, $F_{(3, 36)} = 21.42$, $p < 0.0001$). In *post hoc* analysis of data from both modifier strains, a statistically significant decrease in nuclei counts was observed near the optic nerve head and extended more peripherally in the inferior than in the superior retina (Fig 5J and S1 Data). Importantly, degeneration was limited to areas where dysplastic lesions were observed at one month of age (Fig 4C and 4D) and the peripheral retina was largely spared, as previously reported in STOCK *Crb1^{rd8}* mice [19]. No significant difference in nuclei counts was observed in *post hoc* analysis comparing B6 and B6 *rd8* at 12 months of age, although an age-related decrease in counts throughout the retina was evident in both strains (compare Figs 4J and 5J). Taken together with the histological findings at one month of age, these results establish that dysplastic lesions, neovascular structures, and photoreceptor cell loss occur and progress to different extents among B6 *rd8*, *Tvrm266*, and *Tvrm323* mice, supporting the hypothesis that modifier genes contribute to *Crb1^{rd8}* retinal disease variability.

Cellular disorganization at dysplastic lesions

Retinal dysplasia associated with mutant *Crb1* alleles in mice and rats is characterized by mislocalized photoreceptor cells, shortened photoreceptor outer segments, dysmorphic Müller cells, and the mobilization of immune cells, including microglia and possibly infiltrating macrophages, to the subretinal space [19,35,38,43,51]. Mislocalized rod photoreceptor cells were readily identified in histological sections, as the nuclei of these cells in adult mice are compact and stain intensely with hematoxylin (Fig 4). To assess rod outer segment integrity and to test
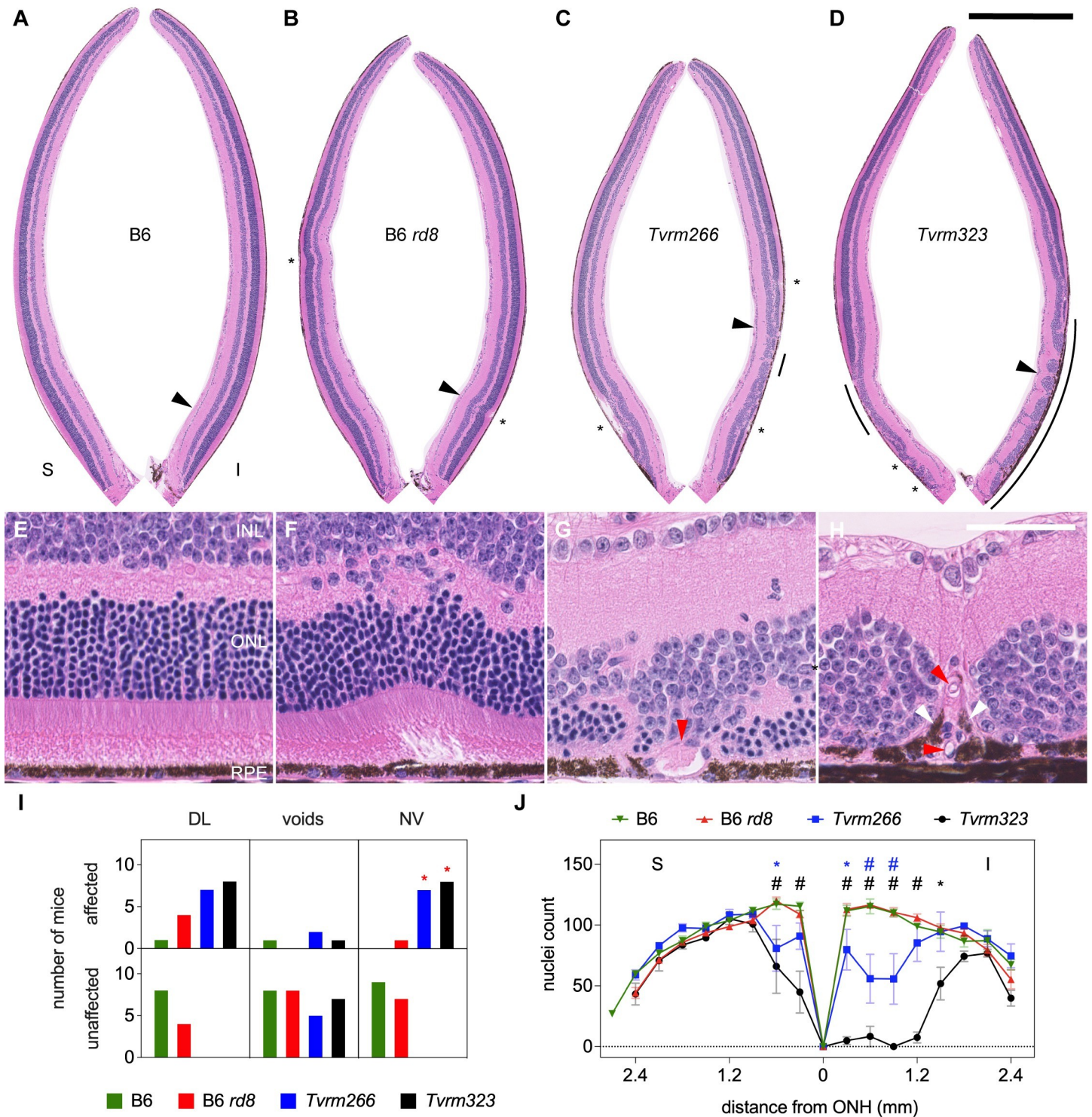
Fig 5. Histological analysis at 12 months of age. A–D. Superior (S) and inferior (I) retinas cropped from representative digital images of B6, B6 *rd8*, *Tvrm266* and *Tvrm323* whole eye sections stained with hematoxylin and eosin and imaged with a slide scanner. Dysplastic lesions, *asterisks*. Areas devoid of photoreceptor nuclei, *solid lines*. Scale bar, 0.5 mm. Sites from A-D detailed in panels E–H, respectively, are marked by *arrowheads*. E. Normal retinal layers in B6 mice, labeled as in Fig 4. F. Dysplastic lesion in B6 *rd8*. G, H. Photoreceptor loss at neovascular lesions (*red arrowheads*) in *Tvrm266*, and *Tvrm323* mice, respectively. In G, red blood cells are observed within a large vessel at the RPE. I. Incidence of pathological features among mice. Samples showing one or more of the identified features among 10–21 sections were scored as affected. DL, dysplastic lesions; NV, neovessels. *Asterisks* denote statistical significance (Fisher's exact test against B6 *rd8* mice, $p < 0.05$). J. Photoreceptor nuclei count within a 50 μm length of retina as a function of distance from the ONH. Values represent mean ± SEM; n = 6–8. Statistical significance colored according to the strain compared to B6 *rd8* in *post hoc* tests. $p < 0.01$, asterisk; $p < 0.0001$, hash symbol.

if other retinal cells were abnormally distributed, immunofluorescence analysis of retinal sections was performed using antibody markers for photoreceptor outer segments, Müller glia, and microglia (Fig 6). Rod and cone outer segments were correctly localized to the outer retina in B6 mice (Fig 6A) and in intact retinal regions of B6 *rd8*, *Tvrm266*, and *Tvrm323* mice (Fig 6B–6D). By contrast, outer segments were absent from the RPE interface at dysplastic lesions in all three mutant strains. Small foci of rhodopsin (RHO) and M opsin (OPN1MW) staining were observed throughout the dysplastic areas, consistent with mislocalization of photoreceptor cells.

In some instances, intact cone outer segments were observed in the interior of pseudorosettes (Fig 6C, *arrowheads*), suggesting infolding of the intact outer retina. In B6 mice, Müller glia were observed with soma positioned at the center of the INL and retina-spanning processes extending to endfeet at the internal limiting membrane (ILM) and ELM (Fig 6E and 6I). Similar morphology was observed in unaffected regions of B6 *rd8*, *Tvrm266*, and *Tvrm323* retinas (Fig 6F–6H), but at dysplastic lesions, Müller cell bodies were occasionally displaced toward the ONL (Fig 6F–6H and 6J–6L *arrowheads*). Müller cell displacement was observed in 2/4 lesions that were imaged in three B6 *rd8* mice, 4/12 lesions in seven *Tvrm266* mice, and 14/18 lesions in seven *Tvrm323* mice. These results suggest that Müller cell displacement is a common feature of dysplastic lesions, particularly those that are more severe as in *Tvrm323* mice. Microglia were found in their normal locations on the outer surface of the INL in B6 mice (Fig 6M) and in unaffected regions of the three *Crb1*^rd8^ strains (Fig 6N–6P). By contrast, at dysplastic lesions of these strains, microglial cells accumulated in the subretinal space or appeared to be displaced toward this region (Fig 6N–6P). P2RY12 staining between the outer plexiform layer and subretinal space indicated displacement of microglial cells and was observed in 4/5 lesions imaged from five B6 *rd8* mice, 7/9 lesions in six *Tvrm266* mice, and 24/24 lesions in eight *Tvrm323* mice. This observation provides evidence for a strong correlation between lesions and displaced microglia. As in other *Crb1* mouse and rat models [19,35,38,43,51], these results emphasize an enhanced focal pathology in *Tvrm266* and *Tvrm323* mice that is limited to dysplastic lesions, in which photoreceptor cells are displaced toward the INL from their normal locations and Müller cells and microglia are mobilized toward the outer retina and RPE.

ELM fragmentation

Pan-retinal disruption of the ELM is a distinct feature of homozygous *Crb1*^rd8^ mice thought to arise from a defect in the formation and maintenance of cell-cell adhesive interactions, which depend on CRB1 [19]. This feature is observed in retinal sections of *Crb1*^rd8^ mutant mice immunostained with antibodies against components of the cell adhesion machinery, such as β-actin, cadherins, PALS1, or TJP1 [19,40], which reveal a fragmented appearance characterized by small gaps in the normally continuous ELM. It is unknown whether retinal dysplasia requires ELM fragmentation or is instead the result of an independent pathological process. To test whether fragmentation was affected by the modifier mutations, we stained retinal sections to detect TJP1. The ELM was continuous in the inferior (Fig 7A) and superior retina (Fig 7E) of B6 mice but exhibited gaps in the corresponding regions of B6 *rd8* (Fig 7, 7B and 7F) and *Tvrm266* mice (Fig 7, 7C and 7G). Strikingly, however, ELM fragmentation was rare in *Tvrm323* retinas (Fig 7, 7D and 7H), despite an increase in the number and size of dysplastic lesions. The decrease in the number of gaps relative to B6 *rd8* was particularly noticeable in the superior retina of *Tvrm323* mice, which at one month of age had no dysplastic lesions (compare Fig 7H and 7F). Note that the ELM is distorted at dysplastic lesions (for example, Fig 7B) and therefore fragmentation cannot be evaluated at these sites. Gap counts normalized to ELM
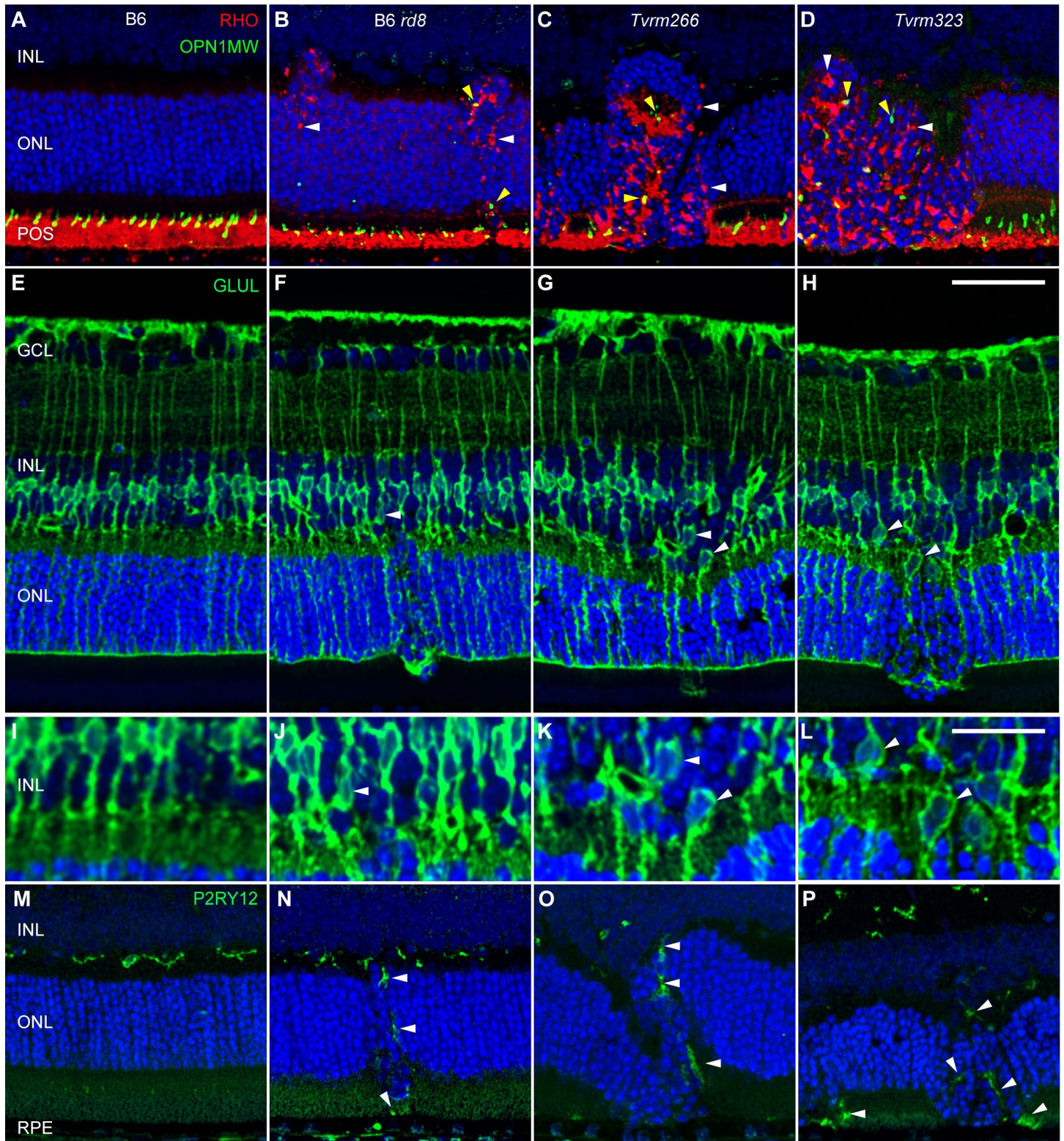
Fig 6. Ectopic retinal cells in dysplastic lesions at one month of age. Retinal sections of 7–9 B6 (A, E, I, M), B6 *rd8* (B, F, J, N), *Tvrm266* (C, G, K, O), and *Tvrm323* (D, H, L, P) mice were examined for each panel of markers studied. A–D. Staining with rhodopsin (RHO, *red*) and M cone opsin (OPN1MW, *green*) antibodies indicated a normal location of rod and cone outer segments in B6 mice (A) but an ectopic location at dysplastic lesions of *Crb1^rd8^* mutants (B–D; *white* and *yellow arrowheads*, respectively). E–H. Glutamine synthetase (GLUL, *green*) antibodies revealed Müller cell soma at the center of the INL in B6 mice (E, detailed in I) but displaced toward the

ONL at lesions of *Crb1^{rd8}* mutants (F–H, *white arrowheads*, detailed in J–L). M–P. Purinergic receptor P2RY12 antibodies (*green*) revealed microglia at their normal location in the OPL of B6 mice but mobilized to the ONL and subretinal space among dysplastic lesions of *Crb1^{rd8}* mutants (*arrowheads*). Nuclei were detected with DAPI (*blue*). Scale bars: H, 50 μm, applies to A–H and M–P; L, 25 μm, applies to I–L.

length in areas unaffected by dysplasia were determined as a measure of fragmentation (Fig 7I and S1 Data). A statistically significant difference in this measure was observed in one or more strains compared to B6 *rd8* (one-way ANOVA, $F_{(3, 12)} = 38.90$, $p < 0.0001$; S1 Data). In *post hoc* analysis corrected for multiple comparisons by Dunnet's test, statistically significant differences in fragmentation were observed in B6 and *Tvrm323* ($p < 0.0001$), but not *Tvrm266* ($p = 0.091$) mice, compared to B6 *rd8* mice (Fig 7I, *asterisks*; S1 Data). These results provide further evidence that genetic modifiers affect *Crb1^{rd8}* phenotypes differentially and raise the possibility that dysplasia and ELM fragmentation may be independent pathological changes arising from the *Crb1^{rd8}* mutation.

We also tested whether the homozygous *Arhgef12^{Tvrm266}* mutation might result in an ELM phenotype in the absence of the homozygous *Crb1^{rd8}* allele. Compared to *Tvrm266* mice, the gap number per mm of ELM in mice bearing the homozygous *Arhgef12^{Tvrm266}* mutation and a heterozygous *Crb1^{rd8}* allele was significantly reduced to a value near zero (S5 Fig). This result indicates that the ELM fragmentation phenotype of *Tvrm266* mice requires homozygous *Crb1^{rd8}* and suggests that the *Arhgef12* mutation does not result in gross changes to the ELM.

Effect of modifiers on neonatal retinal progenitor cell development

Studies of severely dysplastic *Crb1* mutant mice that also carry conditional mutations in *Crb2* targeted to photoreceptor cells, retinal progenitor cells, or Müller glia have revealed defects in early retinal development [43]. In these strains, mitotic progenitor cells of the retinal neuroblastic layer (NBL), which at P1 are normally localized within a narrow band near the RPE, are distributed ectopically throughout the NBL and even reach the ganglion cell layer [43]. To test for ectopic localization of mitotic progenitor cells in our *Crb1^{rd8}* modifier strains, we examined retinal sections at P0 from B6, B6 *rd8*, *Tvrm266*, and *Tvrm323* mice stained with antibodies against phosphohistone H3 (PHH3) (Fig 8), which identifies cells at mitotic prophase and metaphase. Mitotic progenitor cells were similarly positioned at the NBL apical surface of all
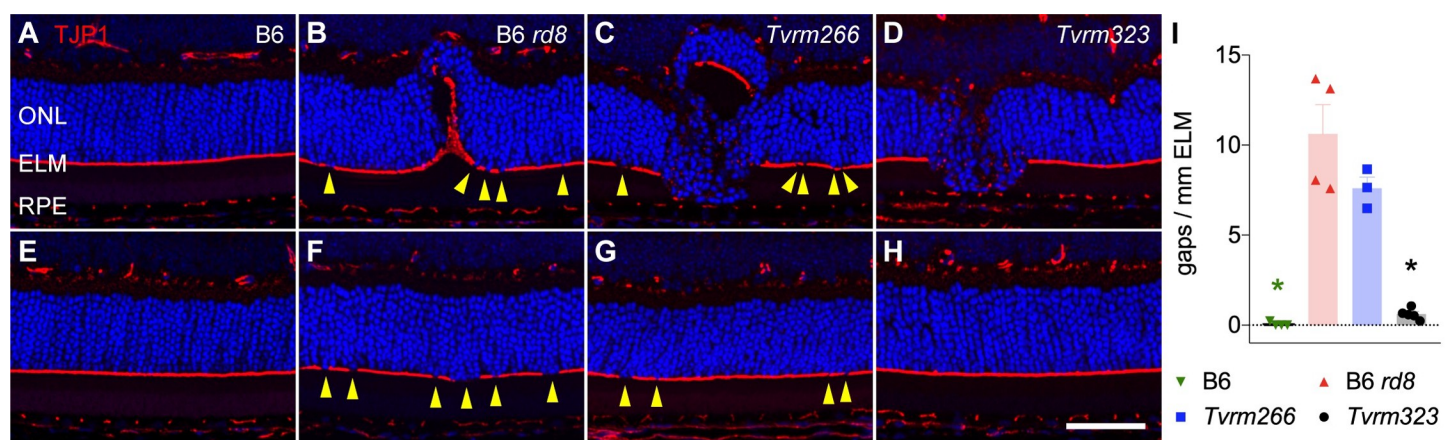
Fig 7. ELM fragmentation in modifier strains. Retinal sections from mice at one month of age were stained with antibodies against TJP1 (*red*) to detect the ELM and DAPI (*blue*) to detect nuclei. A–D. Inferior retina. E–H. Superior retina. A, E, B6; B, F, B6 *rd8*; C, G, *Tvrm266*; D, H, *Tvrm323*. Gaps are indicated by *yellow arrowheads*. Images are representative of n = 8 samples from each strain. H. Scale bar, 50 μm, applies to all image panels. I. Count of gaps over the full length of ELM except at dysplastic lesions, normalized to ELM length (n = 3–4). Bars indicate mean ± SEM. *Asterisks*, $p < 0.0001$, *post hoc* analysis.
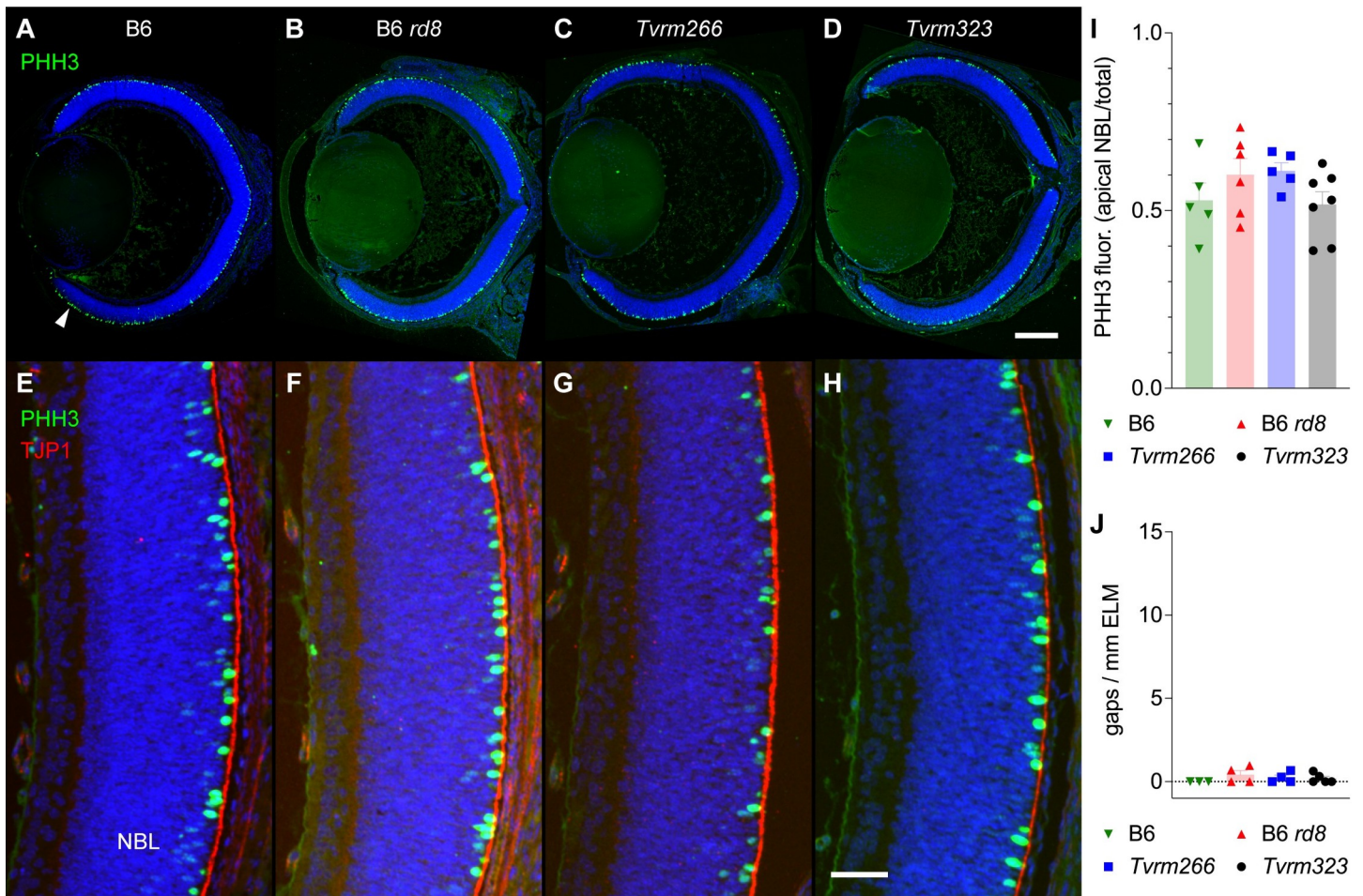
Fig 8. Distribution of mitotic progenitor cells at P0. A–D. Representative ocular sections of B6 (n = 5), B6 *rd8* (n = 6), *Tvrm266* (n = 5), or *Tvrm323* (n = 7) mice, respectively, were probed with antibodies against phosphohistone H3 (PHH3, *red*) to detect mitotic cells and DAPI (*blue*) to detect nuclei. A similar distribution of PHH3-positive staining within the outer NBL (A, *arrow*) was observed in all strains. E–H. Detail of P0 retinas stained as in A–D and with antibody against TJP1 (*red*). The order of samples is the same as in A–D. Placement of progenitor cells undergoing mitosis close to the apical boundary of the NBL, delineated by TJP1, was observed in all strains. NBL, neuroblastic layer. Scale bars: D, 0.25 mm, applies to A–D; H, 50 μm, applies to E–H. I. Quantitation of PHH3 fluorescence in a 20 μm-wide band at the apical NBL relative to the total NBL. J. Quantitation of gaps per mm of the prospective ELM. Bars in I and J indicate mean ± SEM.

https://doi.org/10.1371/journal.pgen.1009798.g008

strains (Fig 8A–8H). Analysis of the PHH3 fluorescence distribution of P0 mice (Fig 8I) revealed no significant difference due to strain (one-way ANOVA, $F_{(3, 19)}$ = 1.48, p = 0.25, n = 3, 6, 5, and 7 for B6, B6 *rd8*, *Tvrm266*, and *Tvrm323*, respectively). Similarly, TJP1 staining, which at P0 detects the prospective ELM, revealed few gaps (Fig 8E–8H). There were no statistically significant differences in the number of gaps per mm of ELM (Fig 8I) due to strain (one-way ANOVA, $F_{(3, 12)}$ = 0.92, p = 0.47, n = 3, 4, 4, and 5 for B6, B6 *rd8*, *Tvrm266*, and *Tvrm323*, respectively). Thus, our analysis does not reject the hypotheses that mitotic progenitor cell localization and prospective ELM integrity at P0 are unaffected by the homozygous *Crb1rd8* mutation alone or in combination with the *Arhgef12* or *Prkci* modifier mutations.

Loss of visual function in modifier strains

Loss of vision in *CRB1*-associated retinal disease occurs congenitally in LCA patients or progresses rapidly during early life in RP and cone-rod dystrophy patients. In comparison, mouse strains carrying a single homozygous *Crb1* mutation exhibit little to no progressive reduction

in visual function as measured by electroretinography (ERG) [20,22,23], limiting their utility as models of *CRB1*-associated vision loss. Functional loss in mouse models is accelerated in strains combining homozygous *Crb1* mutations with modifier mutations, such as those in *Crb2* [42,43,52]. To assess whether a decline in visual function was accelerated in *Crb1*^{rd8} modifier strains, B6, B6 *rd8*, *Tvrm266*, and *Tvrm323* mice were examined by ERG. As no significant loss of photoreceptors was noted histologically at one month of age, scotopic and photopic ERG response amplitudes as a function of flash intensity were measured at four, eight, and 12 months of age (Fig 9A). Scotopic a- and b-wave amplitudes provide a measure of rod photoreceptor and secondary neuron function while the photopic b-wave amplitude measures secondary neuron responses to cone stimulation. Responses at each age were compared statistically to those of B6 *rd8* by mixed-effects analysis, a repeated-measures approach that allows datasets with occasionally missing values. By this analysis (S1 Data), statistically significant differences in mean scotopic a-wave amplitude were detected in one or more strains compared to B6 *rd8* mice (4 months, $p = 0.0306$; 8 months, $p = 0.0022$; 12 months; $p = 0.0004$); in mean scotopic b-wave amplitude (8 months, $p = 0.0009$; 12 months, $p = 0.0002$); and in mean photopic b-wave amplitude (8 months; $p = 0.0034$; 12 months; $p = 0.0021$). *Post hoc* analysis with Dunnet's correction for multiple comparisons revealed a statistically significant decrease in *Tvrm266* a-waves amplitude at a single flash intensity (4 months; -1.8 log cd s/m^2; $p = 0.046$) and in *Tvrm323* at multiple intensities (12 months; -1.4, -1.0, and -0.6 log cd s/m^2; $p = 0.017$, 0.032, and 0.35, respectively). Parallel analysis indicated an unusual and statistically significant increase in mean *Tvrm266* b-wave amplitude (8 months; -1.4, -1.0, and -0.6 log cd s/m^2; $p = 0.031$, 0.013, and 0.0070, respectively) as well as statistically significant decreases in mean *Tvrm323* b-wave amplitude (8 months; 1.8 log cd s/m^2; $p = 0.049$; 12 months; -2.6, -2.2, -1.8, -1.0, and -0.6 log cd s/m^2; $p = .0098$, 0.013, 0.029, 0.013, and 0.0098, respectively). No other comparisons, including those of B6 to B6 *rd8* were found to be statistically significant (S1 Data). These results indicate a transiently increased ERG response in *Tvrm266* mice at eight months of age, which is unexpected in light of the decreased number of photoreceptor cells predicted from histological analysis. They also indicate a loss of photoreceptor function in *Tvrm323* mice as indicated by the statistically significant decrease in scotopic a- and b-wave amplitudes at 12 months of age.

As an alternative measure of progressive functional changes within each strain, we reanalyzed ERG response amplitudes obtained at the highest scotopic and photopic flash intensities as a function of age (Fig 9B and S1 Data). In this analysis, amplitude values at each age were normalized and compared to the mean value at four months of age. Statistically significant differences in response amplitudes at one or more ages were detected in all strains except B6 (S1 Data; two-way ANOVA; scotopic a- and b-wave, photopic c-wave; $p < 0.0001$). *Post hoc* analysis with Dunnet's correction for multiple comparisons revealed a statistically significant decrease in mean B6 *rd8* response amplitudes (12 months; scotopic a-wave; $p = 0.0082$; scotopic b-wave, $p = 0.0020$; photopic b-wave, $p = 0.013$); a statistically significant increase in *Tvrm266* amplitudes (8 months; scotopic a-wave; $p = 0.0001$; scotopic b-wave, $p < 0.0001$) and a statistically significant decrease in *Tvrm323* amplitudes (8 months; scotopic a-wave; $p = 0.0007$; scotopic b-wave, $p < 0.0001$; photopic b-wave, $p = 0.017$; 12 months; scotopic a-wave; $p < 0.0001$; scotopic b-wave, $p < 0.0001$; photopic b-wave, $p < 0.0001$). Comparison of the mean values indicated a progressive and statistically significant decrease in ERG response amplitudes in B6 *rd8* mice of 30–40% from four to 12 months of age, which was exacerbated in *Tvrm323* mice to 44–63% over the same period, consistent with degeneration of rod and cone photoreceptor cells (Fig 9B). *Tvrm266* mice showed increased scotopic responses of 45–51% at eight months of age, a difference which was not sustained at 12 months of age. In summary, the ERG data provide evidence for functional changes in the modifier strains, which differ
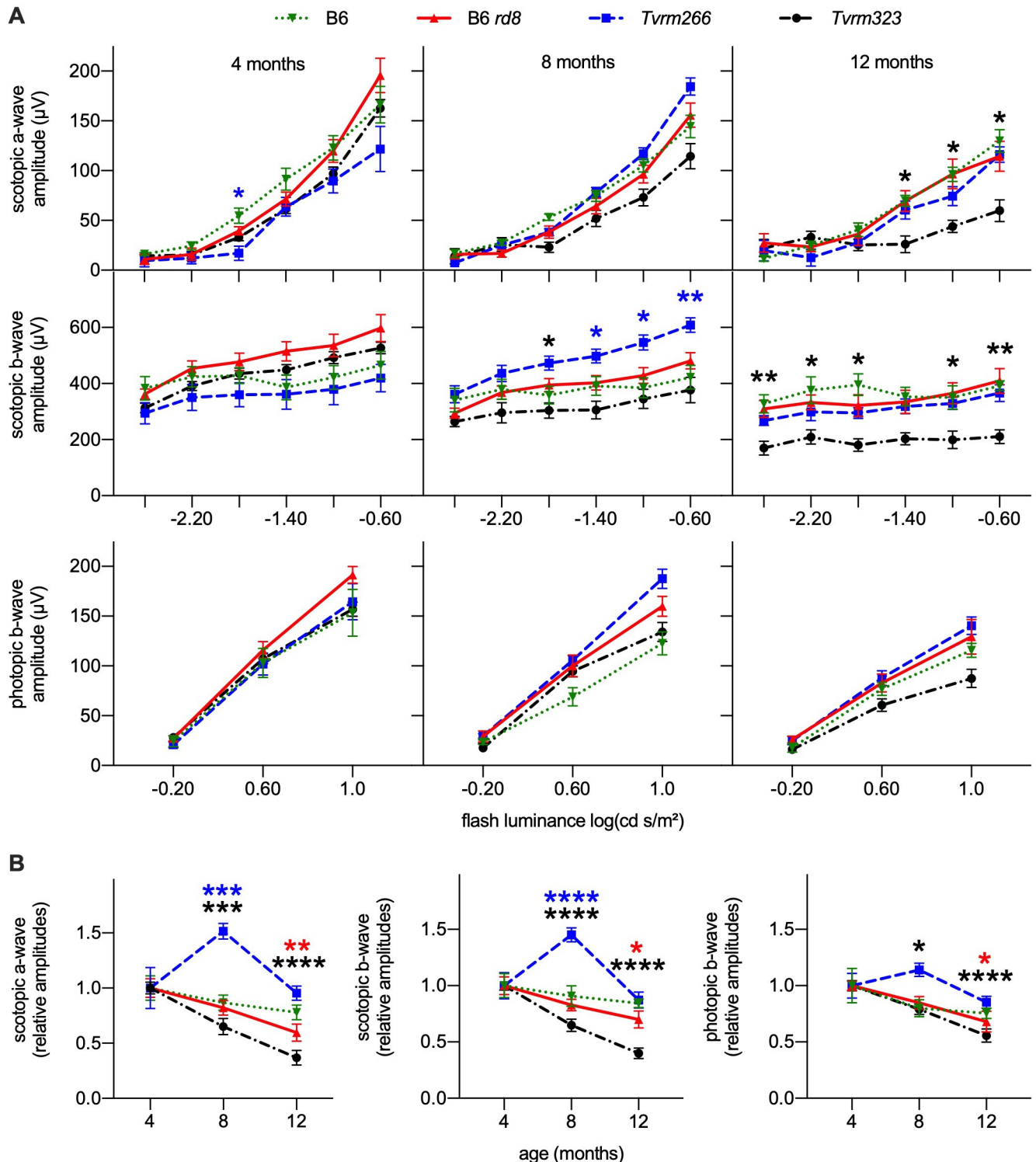
Fig 9. ERG analysis of B6, B6 *rd8*, *Tvrm266*, and *Tvrm323* mice at four, eight, and 12 months of age. A. Scotopic and photopic response amplitudes as a function of flash luminance. *Asterisks* show statistical significance in a comparison to B6 *rd8* and are colored as in the legend to indicate the strain compared. * $p < 0.05$; ** $p < 0.01$. Values indicate mean ± SEM; n = 6–26. B. Response amplitudes at the highest flash luminance as a function of age, normalized to the mean amplitude at four months of age. Legend is the same as in panel A. *Asterisks* indicate statistical significance compared to the value at four months of age and are colored as in the legend in panel A. * $p < 0.05$, ** $p < 0.01$; *** $p < 0.001$; **** $p < 0.0001$.

https://doi.org/10.1371/journal.pgen.1009798.g009

from each other and from B6 *rd8* mice, supporting the hypothesis that *Crb1^{rd8}* modifiers differentially affect retinal function.

Discussion

Modifier genes can alter the onset, progression, severity, and specific characteristics of monogenic ocular diseases, presenting challenges for patient diagnosis, prognosis, and treatment [7,33]. Our finding that mutations in murine *Arhgef12* and *Prkci* modulate *Crb1^{rd8}* retinal phenotypes to differing extents and with different lesion characteristics further supports the hypothesis that modifier gene variants contribute to clinical variability in *CRB1*-associated retinal dystrophy. Our results provide insight as to the pathogenic process and expand the growing network of *Crb1^{rd8}* modifier genes that may ultimately lead to a greater understanding of underlying disease mechanisms that lead to the vast array of CRB1 associated disease phenotypes. The models reported here present with new retinal phenotypes, which more closely recapitulate the human disease and may be useful for pre-clinical studies.

Defects in a number of apicobasal polarity proteins have been observed to cause retinal dysplasia. Three conserved protein complexes first identified in invertebrates are thought to determine apicobasal polarity in epithelial cells and other polarized cell types: the *Drosophila* Crb-Sdt-Patj complex [mouse orthologs CRB(1–3)-MPP5- PATJ], the *Drosophila* Baz-aPKC-Par-6 complex [PARD3(or PARD3B)-PRKC(I or Z)-PARD6(A, B, or G)], and the *Drosophila* Scrib-Dlg1-L(2)gl complex [SCRIB-DLG(1–5)-LLGL(1 or 2)] [53–55]. These complexes direct the formation of cell-cell adhesion complexes, including tight and adherens junctions that further establish the apical, lateral, and basal domains of epithelial cells [56]. Members of the Rho family of small signaling GTPases are also important for the establishment and maintenance of epithelial apicobasal polarity [56–59]. For example, *Drosophila* Cdc42 is responsible for the membrane localization and apical accumulation of Baz, aPKC, Par-6 and Crb, and may mediate exchange of the aPKC-Par-6 subcomplex from Baz to Crb [49]. By contrast, *Drosophila* Rho function is required for cytoskeletal remodeling that stabilizes cadherin-based cell-cell adhesion and reinforces apicobasal polarity [60]. In vertebrate models, mutation or loss of zebrafish (*Danio rerio*) orthologs of apicobasal polarity proteins EPB41L5 (zebrafish moe) [61,62], MPP5 (nok) [63], and CRB2 (ome) [64] cause retinal developmental and lamination abnormalities similar to *Crb1*-associated retinal dysplasia. Deficits in mouse CRB1 [19,20,23], CRB2 [65–67], CRB1 and CRB2 combined [42,52,67], MPP5 [68], and PRKCI [69] have similar effects, supporting the hypothesis that defects in apicobasal polarity cause retinal dysplasia.

Our results also support this hypothesis. Retinal dysplasia is more severe in *Tvrm323* mice, which express variants of two apicobasal polarity proteins, PRKCI and CRB1, when compared to B6 *rd8* mice, in which only CRB1 is disrupted. Our epistasis analysis demonstrated a genetic interaction between *Prkci* and *Crb1* in retinal dysplasia, consistent with known interactions between PRKCI and CRB1 in apicobasal polarity [53–55]. *Prkci^{Tvrm323}* is a novel missense allele, so it is informative to consider its effect on PRKCI function. As ablation of *Prkci* in mice results in lethality by embryonic day 9 [70], the normal viability of homozygous *Prkci^{Tvrm323}* mice suggests that the mutant allele does not compromise PRKCI functions required for growth and survival. Likewise, in the absence of the homozygous *Crb1^{rd8}* mutation, mice carrying the *Prkci^{Tvrm323}* allele do not appear to cause retinal dysplasia, unlike conditional mutants that ablate the gene in differentiating, post-mitotic photoreceptor cells, resulting in severe retinal dysplasia [69]. Moreover, accumulation of PRKCI in *Tvrm323* and B6 eyecups does not differ significantly, indicating that the mutation has little effect on protein synthesis or turnover. The *Prkci^{Tvrm323}* mutation results in substitution of asparagine for tyrosine at amino acid position 136 of PRKCI, which has been identified as a phosphorylated

residue in independent phosphoproteomic studies (PhosphoSite, accessed March 9, 2022). This position lies between a pseudosubtrate sequence (PSR, residues 124–134) and adjacent conserved domain (C1, 141–193) (NCBI Gene, accessed March 9, 2022). Studies of the closely related atypical protein kinase PRKCZ indicate that the tandem PSR and C1 domains bind and allosterically regulate the kinase catalytic domain [71], and studies of both PRKCI and PRKCZ indicate that the C1 domain also controls the binding and response of these enzymes to signaling lipids, such as phosphatidylserine, phosphatidic acid, and phosphatidylinositol monophosphates [72]. Together with our observations, these findings raise the possibility that the *Tvrm323* phenotype results from disruption of a signaling pathway evoked in response to the *Crb1rd8* mutation, in which phosphorylation of PRKCI residue 136 alters the enzymatic autoregulation of PRKCI and/or its binding to signaling lipids. PRKCI kinase function is critical for apicobasal polarity and adherens junction formation [73], and alteration of kinase autoregulation may disrupt these processes. Alteration of lipid binding may also affect PRKCI membrane localization and, by analogy with the apicobasal polarity processes in *Drosophila* discussed above, may disrupt PRKCI association with a PARD6A, B, or G isoform and/or binding of the resulting complex to CRB1.

Our results also point to disruption of a Rho GTPase-mediated apicobasal polarity process in *Crb1rd8* retinal dysplasia. Epistatic analysis revealed a genetic interaction between *Arhgef12* and *Crb1* alleles that led to enhanced retinal dysplasia, suggesting that both genes participate in the same pathogenic pathway. ARHGEF12 protein was undetectable in *Tvrm266* eyecups, suggesting that *Arhgef12Tvrm266* is a null allele. ARHGEF12 (also known as LARG) belongs to the Dbl protein family of guanine nucleotide exchange factors, which are defined by a diffuse B-cell lymphoma (Dbl)-homology domain that activates Rho GTPases by exchanging bound GDP for GTP [74–76]. ARHGEF12 preferentially activates RHOA and to a lesser extent RHOB and RHOC [76–79], potentially affecting their function in apicobasal polarity [56–59]. Several reports suggest ARHGEF12 interacts with Rho GTPases to regulate actin remodeling at sites of cell-cell adhesion. ARHGEF12 is a component of the E-cadherin adhesome defined by proximity proteomics in human gastric adenocarcinoma cells, an epithelial cell model [80]. ARHGEF12 colocalizes and physically interacts with WTIP, an adaptor protein required for stabilizing cell-cell adhesions as they form in mouse renal podocytes [81]. In cultured human cells, ARHGEF12 mediates RHOA-CDC42 cross-talk in a complex with two other Dbl proteins, ARHGEF11 and PLEKHG4B [79], which directs actin remodeling at cell-cell junctions as they mature [82]. Interestingly, ARHGEF12 guanine nucleotide exchange activity requires interaction with the activated α subunits of heterotrimeric G proteins, $G_{\alpha12}$, $G_{\alpha13}$, and $G_{\alpha q}$ [77,78,83–85] and are therefore regulated by the stimulation of G protein coupled receptors (GPCRs) that activate these subunits [85–87]. Together with our results, these observations lead us to propose that a GPCR agonist generated in response to the homozygous *Crb1rd8* defect stimulates ARHGEF12 activation of a Rho GTPase, which may promote actin remodeling at cell-cell junctions to reinforce cell apicobasal polarity. Accordingly, the loss of ARHGEF12 in *Tvrm266* mice would abolish this response and exacerbate retinal dysplasia. Thus, our findings raise the possibility that the increased dysplasia of *Tvrm266* mice is due to combined defects in two proteins that influence apicobasal polarity, CRB1 and ARHGEF12.

An open question is how the genetic interactions of *Arhgef12* and *Prkci* with *Crb1* are mediated at the cellular level. While it is conceivable that dysplasia is due to dysfunction or loss of the encoded proteins in a single cell type, available evidence suggests that the proteins are expressed in multiple cell types, which furthermore may vary developmentally. Retinal CRB1 has been detected in both Müller and photoreceptor cells [16,19], only Müller cells [88], or separately in Müller and photoreceptor cells depending on whether CRB1-A, CRB1-B, or both isoforms were targeted by the antibody used [21]. *Crb1* transcripts are detected in retinal

progenitor cells is expressed starting at embryonic day 11.5 [89]. *Crb1* is also expressed in vascular endothelial cells of the mouse retina and upregulated under conditions associated with increased endothelial cell polarization [90]. Mouse PRKCI is widely distributed among retinal progenitor cells at the apical surface of the NBL at P0, but mainly in the inner nuclear and ganglion cell layers at P9 [69]. Like *Crb1*, *Prkci* transcripts are detected in retinal endothelial cells and increase in abundance with cell polarization [90]. There is genetic evidence that PRKCI functions in these cells [91]. Retinal endothelial cells also express *Arhgef12* transcripts during postnatal angiogenesis in mice at P8 [92]. From single-cell RNA sequencing online resources (The Broad Institute Single Cell Portal, https://singlecell.broadinstitute.org/single_cell, accessed March 12, 2022), *Arhgef12* transcripts were observed in retinal progenitor cells at embryonic day 13.5 [93] and in amacrine, horizontal, and ganglion cells, astrocytes, fibroblasts, pericytes, and vascular endothelium at P14 [94], while *Prkci* transcripts were detected in horizontal cells [94]. Although these studies support the hypothesis that apicobasal polarity defects in retinal progenitor cells cause retinal dysplasia, the observation that *Arhgef12*, *Prkci*, and *Crb1* genes are expressed in retinal endothelial cells raises the intriguing possibility that vascular cell polarity defects may also contribute to the disease. Further studies to resolve the pathogenic roles of specific retinal cell types expressing these proteins are needed to advance our understanding of disease mechanisms.

The phenotypes observed in *Tvrm266* and *Tvrm323* mice provide important insights regarding the pathogenic process(es) leading to retinal dysplasia. First, photoreceptor cell nuclei and outer segments are mislocalized only at dysplastic lesions. Second, in dysplastic lesions of both models and B6 *rd8* mice, Müller cell soma are displaced from their normal location in the center of the inner nuclear layer toward the RPE. Similar displacement has been observed in other murine retinal injury models [95,96]. Third, compared to B6 control animals, microglia at lesions are mobilized toward the subretinal space in both modifier strains and in B6 *rd8* mice. Similar immune cell mobilization observed in other homozygous *Crb1^rd8* strains [35,38,43] may indicate a contribution of these cells to lesion formation, although direct tests of this hypothesis have not been reported. Fourth, ELM fragmentation, which arises from a focal loss of cell-cell adhesion among Müller and photoreceptor cells, is reduced in *Tvrm323* mice compared to *Tvrm266* and B6 *rd8* mice, despite increased dysplasia. This result raises the possibility that ELM fragmentation and retinal dysplasia are independent phenotypes associated with *Crb1* mutation, in agreement with previous observations that dysplasia can be suppressed without affecting fragmentation [19] and that certain *Crb1* mutants exhibit dysplasia while retaining an ELM structure similar to that of wild-type controls [20]. Fifth, cyst-like structures within the outer nuclear layer of both models accumulate in the region of the retina where dysplastic lesions occur. These structures may be related to foveolar retinoschisis [97] or macular edema [98], often detected in *CRB1* RP patients [25,99]. The cause of these cyst-like structures is unknown but, based on the observation of vascular leaks upon Müller cell ablation [100], they may ultimately arise from defects in junctions between Müller cells and retinal vascular beds. Finally, in *Tvrm266* and *Tvrm323* mice at both one month and one year of age, vascular structures are observed in dysplastic regions, some of which include displaced RPE cells. Vascular structures related to retinal angiomatous proliferation are observed in other *Crb1* mutant modifier strains [38,39,41,43], and macular telangiectasia-like structures have been reported in a rat *Crb1* mutant [51]. Taken together, these results suggest a pathogenic process in which disruption of apicobasal polarity complexes results in abnormal activation of Müller, immune, and vascular cells, leading to edema, neovascular changes, and focal tissue remodeling observed as dysplastic lesions. Further studies of *Tvrm266* and *Tvrm323* mice may help elucidate the molecular mechanisms that underlie this process.

Our results add to a growing list of reported *Crb1^rd8* modifier genes, which include *Cx3cr1*, *Mthfr*, *Crb2*, *Cygb*, *Jak3*, and *Nfe2l2* [35,39–43,45]. Analysis of modifier genes in mouse models of other diseases have been useful for assembling genetic networks that provide important clues to pathogenesis and offer new avenues for therapeutic intervention [31,32]. As discussed above, *Crb1*, *Crb2*, *Arhgef12*, and *Prkci* may be placed in a network of apicobasal polarity genes. However, it is not obvious how the remaining modifier genes identified to date fit into this network. *Cx3cr1* encodes an immune-cell receptor for fractalkine, a signaling molecule expressed predominantly in the central nervous system and upregulated in injured neurons [101]. *Mthfr* encodes 5,10-methylenetetrahydrofolate reductase, a folate metabolic enzyme that influences serum homocysteine levels and is implicated in diverse conditions, including neurodegenerative disease [102]. *Cygb* encodes cytoglobin B, an oxygen-binding protein expressed in vascular pericytes that may protect against cellular oxidative damage [103]. *Jak3* encodes a signaling kinase that regulates myeloid and lymphoid cell development and activation [104,105], and *Nfe2l2* encodes a transcriptional factor in many cell types that regulates oxidative stress genes [106]. Although all these genes can conceivably be associated with the phenotypes we observe, identifying additional genes that fill in missing connections will be necessary to construct a comprehensive network to explain retinal dysplasia. Our study has highlighted the utility of a sensitized mutagenesis screen to identify *Crb1^rd8* modifier genes, which will continue to extend the network. These efforts may be amplified by the characterization of retinal dysplasia among B6N-derived strains generated by the Knockout Mouse Phenotyping Program and International Mouse Phenotyping Consortium, where every knock-out line also bears the *Crb1^rd8* mutation [107, 108]. The potential of this second approach has been demonstrated [40].

The identification of *Arhgef12* and *Prkci* as *Crb1* modifier genes in mice may have relevance to diagnosing and developing treatments for human *CRB1*-associated retinal disease. Some patients possessing a single identified *CRB1* variant allele may be affected due to modifier gene variants [2]. For example, it has been suggested that *CRB2* variants may modify *CRB1* alleles in humans [42,43]. The increased retinal dysplastic phenotype of conditional *Crb2* mutant mice carrying heterozygous *Crb1* knockout alleles [42,43] suggests this effect could occur among patients bearing a single mutant *CRB1* allele. Thus, identifying *Crb1* modifiers in mice, such as *Arhgef12* and *Prkci*, may provide gene candidates for diagnostic screening of patients who retain only a single mutant *CRB1* allele. In addition, the altered disease characteristics caused by *Crb1* modifier genes, including but not limited to *Arhgef12* and *Prkci*, may aid in disease prognosis. If disruptive variants of mouse *Crb1* modifier genes are found in *CRB1* patients, a better prediction of disease onset, progression, severity and specific pathological features might be possible based on the corresponding murine phenotypes. Further, the mouse models described here exhibit new features aligned with human *CRB1* pathology, which may aid in developing therapies. The cyst-like lesions in both *Tvrm266* and *Tvrm323* mice may be useful for understanding the origin of and testing treatments for macular and foveal retinoschisis associated with *CRB1* variants [25,97–99]. The progressive decline in rod and cone cell ERG responses in *Tvrm323* mice is faster than in mice carrying a single homozygous *Crb1* mutation, including STOCK *Crb1^rd8* mice, and may be useful for understanding and treating functional decline in *CRB1* patients. Translational studies using these *Crb1^rd8* modifier mouse models, which are readily available to researchers, may yield insights that improve the care of patients affected by *CRB1*-dependent retinal dystrophy.

Methods and materials

Ethics statement

All procedures utilizing live mice were approved by the JAX Institutional Animal Care and Use Committee (protocol ACUC 99089).

Colony management and ENU mutagenesis

STOCK $Crb1^{rd8}$ mice were backcrossed to C57BL/6J (JAX stock number 000664) mice for seven generations to produce an incipient congenic strain, B6.Cg-$Crb1^{rd8}$/Pjn (N_7), which was bred to homozygosity. Males from this incipient congenic colony were administered weekly intraperitoneal injections of ENU (Millipore Sigma, Burlington, MA, USA; N3385) for three consecutive weeks at a concentration of 80 mg/kg per treatment [109,110]. Following return to fertility, the mutagenized G_0 males were backcrossed to B6.Cg-$Crb1^{rd8}$/Pjn females, producing G_1 mice which were subsequently outcrossed to unmutagenized B6.Cg-$Crb1^{rd8}$/Pjn (N_7) and resulting female G_2 mice were backcrossed to G_1 sires to produce G_3 mice [46].

G_3 mice were screened at 12 weeks of age using indirect ophthalmoscopy. Heritability of novel ocular phenotypes was established by outcrossing to B6.Cg-$Crb1^{rd8}$/Pjn (N_7) mice, producing F_1 progeny to test for dominance. If no phenotype was observed, F_1 mice were then intercrossed, to produce F_2 progeny, and screened for recessive phenotypes. Once heritability was established, mutant mice were assigned a number in the TVRM program [46] and lines were bred and maintained in the JAX Research Animal Facility. Mutant strains were backcrossed five generations (N_5) to the founder strain, B6.Cg-$Crb1^{rd8}$/Pjn, to remove potential unlinked mutations before samples for characterization were collected. The full designations for the modifier strains are B6.Cg-$Crb1^{rd8}$ $Arhgef12^{Tvrm266}$/Pjn and B6.Cg-$Crb1^{rd8}$ $Prkci^{Tvrm323}$/Pjn, which are abbreviated as *Tvrm266* and *Tvrm323*, respectively, and refer to a genotype that is homozygous for both $Crb1^{rd8}$ and the modifier allele unless otherwise indicated.

Mice were provided with NIH 6% fat chow diet and acidified water, with a 12:12 hour dark: light cycle in pressurized individual ventilation caging and were monitored regularly to maintain a pathogen-free environment.

Fundus photodocumentation

Mouse pupils were dilated using 1% Cyclomydril (Alcon) prior to imaging. Isoflurane (Kent Scientific) was delivered at 2–4% with an oxygen flow rate of 0.5 liter/min to anesthetize mice during imaging. Color fundus videos (100 frames) were acquired using a Micron IV Retinal Imaging Microscope (Phoenix Technology Group), and registered, averaged, and sharpened in Fiji [111] using the ImageStabilizeMicronStack macro as described [112]. Images were further processed using a custom Fiji macro that applies the Polynomial Shading Corrector plugin (degree x = 2, degree y = 2, regularization = 50) to flatten brightness across the image and resets the range of each channel to optimize color balance.

Gene identification

Based on observations during initial breeding, the mutations in *Tvrm266* and *Tvrm323* appeared to segregate as semidominant alleles. To determine the map position of *Tvrm323*, affected mice (enhanced spots) were outcrossed to C57BL/6NJ (B6N, JAX stock number 005304) and the resulting F_1 progeny were backcrossed to B6N. All backcross progeny homozygous for the $Crb1^{rd8}$ mutation were phenotyped by indirect ophthalmoscopy. DNA from 103 backcross progeny (59 unaffected, 44 enhanced) were genotyped with 149 single nucleotide polymorphisms (B6/B6N SNP panel) spanning the genome (JAX Fine Mapping Facility). We identified genomic regions where >70% of the B6 allele co-segregated with the enhanced phenotype. Candidate genes for *Tvrm323* were identified in the minimal confidence interval on Chr 3. Gene-specific PCR amplification and subsequent Sanger sequencing confirmed a missense mutation in *Prkci*. To identify the causative mutation in *Tvrm266*, high-throughput exome sequencing was performed on a whole-exome library created from *Tvrm266* genomic

DNA on a HiSeq 2000 Sequencing System (Illumina) as previously described [113]. Whole-exome sequencing of *Tvrm266* identified a nonsense mutation in *Arhgef12*, which was subsequently confirmed by Sanger sequencing. An abbreviated mapping cross, with 16 progeny (8 unaffected, 8 enhanced) confirmed the cosegregation of the affected *Tvrm266* phenotype with the *Arhgef12* mutation on Chr 9.

For strain maintenance, modifier mice were genotyped using DNA isolated from tail tips incubated with 50 mM sodium hydroxide at 95˚C for about 20 min before being neutralized with 1M Tris-Cl, pH 8.0, to a final concentration of 50 mM. PCR amplification was performed in a 10 μl reaction volume containing 1X PCR Buffer (New England Biolabs), 10 μM dNTP and 0.05 U Taq DNA polymerase (New England Biolabs). An initial denaturation step at 97˚C for 2 minutes was followed by 45 cycles of 10 seconds at 95˚C, 15 seconds at 55˚C, and 30 seconds at 72˚C with a final 3 minute extension at 72˚C. *Prkci* genotypes were determined using an allele-specific protocol combining the following primers (Eurofins Genomics): Prkci-F, TCCAGCAGTAAGTATGGGAAAC; Prkci-WT-R, GTGTGGCCATTTGCACAACA; and Prkci-MUT-R2, GTTTGGCTTGAAAAACGTGGCCATTTGCACAGTT. Depending on zygosity, this protocol yielded amplified products of 145 bp (WT), 159 bp (mutant), or both. *Arhgef12* genotypes were determined by direct sequencing. DNA samples were amplified with primers (Arhgef12-266seqF, CACACACACGTCACTGTAAA; mArhgef12-266seqR, GAGTGCCTCAATCCACATAAG). The PCR products were purified and sequenced using the reverse primer.

Western analysis

B6, B6 *rd8*, *Tvrm266*, and *Tvrm323* mice (n = 4) adult eyes at approximately two months of age were dissected in ice-cold PBS with EDTA-free protease inhibitor cocktail (Roche) to remove the anterior eye and lens, and snap-frozen in eppendorf tubes on dry ice. Eyecups were combined with 100 μl 1× NuPAGE LDS sample buffer/reducing agent (Invitrogen), homogenized immediately using a hand-held pellet pestle motor (Kontes) on ice, and briefly sonicated (Qsonica). Lysates were then centrifuged briefly at 16,000g. A dilution series of the B6 samples was used to standardize the western signal. For eyecups at one month of age (S3 Fig) were combined with ice-cold RIPA buffer (1% NP-40, 0.5% sodium deoxycholate, 0.1% sodium dodecyl sulfate) containing EDTA-free protease inhibitor cocktail, homogenized, and centrifuged for 20 min at 16,000g. The supernatant was collected and protein concentration determined by Protein Assay reagent (Bio-Rad) using a DU530 spectrophotometer (Beckman Coulter). For each sample, 20 μg was analyzed by gel electrophoresis. Samples were denatured at 100˚C for 10 min and electrophoresed on a 10% Mini-Protean TGX gel (Bio-Rad). Electrophoresed proteins were transferred onto a nitrocellulose membrane using Turbo-blot Transfer system (Bio-Rad). Membranes were pre-blocked in Blotto A (5% w/v milk powder in Tris-buffered saline, 0.05% Tween [TBS-T]), and incubated with antibodies against ARHGEF12 (Santa Cruz, sc-15439), PRKCI (Novus, NBP1-84959), or GAPDH (Cell Signaling, #2118) at 4˚C overnight. Membranes were washed in TBS-T and incubated with HRP-conjugated anti-goat IgG (R&D, HAF017) or anti-rabbit IgG (Cell Signaling, 7074S) antibody in Blotto A (1:1000) for 2 h at room temperature. Following washes in TBS-T, immunoblots were visualized using the Clarity ECLWestern Blot Detection System (Bio-Rad). Protein band images in 16-bit tif format were captured using an Azure c600 bioimaging system (Azure Biosystems). The raw integrated densities of the ARHGEF12 or PRKCI bands, and the densities for GAPDH bands on the same blots, were determined using Fiji following subtraction of a constant background value evaluated between lanes. The density values for the standard series were plotted against load volume and fit to a hyperbolic curve in Prism, which was used to

calculate the relative load volumes for all samples. Relative expression was determined by dividing the equivalent load volumes of the ARHGEF12 or PRKCI bands by those of the corresponding GAPDH bands. The resulting values were normalized by dividing by the mean ARHGEF12 or PRKCI values from all B6 samples.

RNA extraction and analysis

Total RNA was extracted from B6, B6 *rd8*, *Tvrm266*, and *Tvrm323* mice (n = 5) at one month of age by homogenizing posterior eyecups in TRIzol (Thermo Fisher) using a gentleMACS dissociator (Milteny Biotec). Chloroform was then added and the resulting aqueous phase transferred to 100% ethanol. RNA clean-up was performed using an RNeasy spin column kit (Qiagen). DNase (Qiagen) treatment was performed according to the manufacturer's instructions. Total RNA was eluted in RNase-free water, quantified using a NanoDrop ND1000 spectrophotometer (Thermo Fisher) and examined for quality using the TapeStation 4150 system (Agilent Technologies). cDNA was synthesized using the Superscript IV Firststrand Synthesis kit (Thermo Fisher).

To design primers for use in real time quantitative PCR, gene and coding sequences were downloaded from mouse Ensembl (https://useast.ensembl.org). Forward and reverse primers amplifying cDNA sequences of 150–250 bp and separated by large intronic regions in the genomic sequence were designed using Primer3 software (http://bioinfo.ut.ee/primer3-0.4.0/), which yielded Arhgef12 rt-F3 (AGAGCCATCAGTCACTGGACA) and Arhgef12 rt-R3 (CAGCCGTTCCTGTTCCTTTC) for *Arhgef12*, and Prkci rt-F1 (GGAGTGAGGAGATGCC GAC) and Prkci rt-R1 (TCATAATATCCCCGCGGTAG) for *Prkci*. For quantitative RT-PCR, amplification using these primers was performed with iTaq Universal SYBR Supermix (Bio-Rad Laboratories) using the CFX96 Real-time PCR Detection System (Bio-Rad). The relative fold change of gene transcripts was calculated using the comparative CT method ($\Delta\Delta C_T$), and $2^{-\Delta\Delta CT}$ values were normalized to levels of *Actb*, an internal control calibrator. Melting curve analysis was evaluated to confirm accurate amplification of the target genes.

Histological analysis

Following carbon dioxide euthanasia, eyes were enucleated, placed in chilled methanol:acetic acid:phosphate-buffered saline (PBS) (3:1:4), fixed overnight at 4˚C, and stored in 70% ethanol. Fixed eyes were embedded in paraffin and 5 μm sections were stained with hematoxylin and eosin or left unstained for immunohistochemistry (see below). Eyes were oriented to yield sections parallel to the superior-inferior axis by marking the superior eye with a non-soluble paint prior to enucleation. Eyes were also oriented using the long posterior ciliary arteries, which serve as landmarks [114] and could be viewed from the back of embedded eyes illuminated through the cornea. Histosections were scanned using a NanoZoomer 2.0-HT digital slide scanner (Hamamatsu) at 40× magnification; typically 18–21 sections were captured per slide. Sections on the slide were reviewed using NDP.view 2 software (Hamamatsu) to ensure correct orientation based on the position of the central retinal artery to one side of Bruch's membrane opening at the optic nerve head. All sections were reviewed for the presence of pathological features, including dysplastic lesions, voids, or neovessels, and mice were graded as affected if the feature was observed in one or more sections. To address whether voids were an artifact of histological fixation, we reviewed NanoZoomer images from B6 eyes collected at 0.9–1.1 months of age over a period of nine years and found that no voids were present. To assess photoreceptor cell loss from scanned images, a custom Fiji macro was first used to extract .tif images of single sections from full-resolution NanoZoomer output files. A separate macro was created to draw tilted rectangular regions of interest (ROIs) encompassing a 50 μm

length of retina and spaced at 0.3 mm intervals starting from the optic nerve head. Photoreceptor cell loss was determined from .tif images by manually counting photoreceptor cell nuclei within each ROI.

Immunohistochemistry

Unstained sections of eyes were deparaffinized through a xylene/alcohol gradient series. Following deparaffinization, antigen retrieval was performed by microwave treatment for 6 min in 10 mM sodium citrate. Samples were treated with blocking solution (1:50 normal donkey serum:PBS, 0.3% v/v Triton X-100) for 30 min at room temperature and then incubated overnight at 4°C with primary antibodies against rhodopsin (MS-1233-R7, Thermo Fisher), green opsin (AB5405, EMD Millipore), glutamine synthetase (ab176562, Abcam), phosphohistone H3 (PHH3; ab14955, Abcam), P2YR12, (AS-55043A, AnaSpec), and TJP1 (339100 and 61–7300, Thermo Fisher), all diluted 1:100 in blocking solution. Slides were washed using 1× PBS prior to application of secondary antibodies at 1:200 in blocking solution for two h at room temperature. Nuclei were stained using DAPI (10 μg/ml in PBS) for 5 min. Negative controls, in which primary antibodies were omitted during the incubation stage, were performed in parallel. All samples were mounted in Vectashield (Vector Laboratories), coverslipped and imaged using a Zeiss Axio Observer.z1 fluorescence microscope (Carl Zeiss Microscopy) with an ApoTome2 attachment. To count ELM gaps, ApoTome2 stacks encompassing the full thickness of the stained section and covering the entire retina were acquired and processed to yield a maximum intensity projection using Zen 2.6 software (Carl Zeiss). The resulting images were viewed in Fiji and gaps counted manually. The ELM was manually fit to a spline curve, avoiding dysplastic regions identified in the DAPI channel. The gap count was divided by the total ELM length calculated from the fitted curves. To assess the distribution of mitotic nuclei at P0, images were acquired with a 10× objective using the Zeiss microscope and ApoTome, and analyzed in Fiji to compare the intensity of PHH3 fluorescence at the apical NBL to that in the full NBL as described previously [115].

ERG analysis

ERG analysis was carried out using a Espion V6 ColorDome Multifocal system (Diagnosys) essentially as described [116]. Mice at four, eight, and 12 months of age were dark-adapted overnight and pupils were dilated using 1% atropine sulfate (Akorn) or 1% cyclopentolate (Akorn). Mice were anesthetized using ketamine (Covetrus) and xylazine (Akorn) diluted in normal saline and administered by intraperitoneal injection at a final dose of 80 and 16 mg/kg of body weight, respectively. Anesthetized mice were placed on the heated platform of the Espion system. Gold loop electrodes were placed on the corneal surface of each eye along with Goniovisc hypromellose ophthalmic solution (HUB Pharmaceuticals), Gonak (Akorn), or Refresh (Allergan). Small needle electrodes beneath the skin at the top of the head and at the tail served as reference and system ground, respectively. Eyes of dark-adapted mice were presented with a six-step protocol of increasing light intensity measuring mainly rod-dependent responses, followed by light adaptation and a three-step protocol measuring cone-dependent responses. The flash luminance (cd s m^{-2}), number of sweeps, and time between sweeps (s) for the dark-adapted series was 0.0025, 5, 5; 0.006, 5, 5; 0.016, 5, 5; 0.04, 5, 10; 0.1, 5, 15; and 0.25, 5, 15, respectively. Following a 10-min light adaptation at 110 cd/m^2, the corresponding parameters for the light-adapted series were 0.63, 10, 1; 4, 10, 1; and 10, 20, 1 on a background illumination of 110 cd m^{-2}. Response amplitudes were determined from the average of multiple sweeps as follows: scotopic a-wave, pre-flash baseline to the negative trough; scotopic b-wave, negative trough to positive peak within 40–120 ms following the flash; photopic

b-wave, negative trough to positive peak within 40–60 ms following the flash. The mean response amplitude from both eyes of each mouse was used for statistical analysis; if data were missing from one eye, only one eye was used.

Statistical analysis

Genotype-phenotype associations to identify the causative mutation and to determine the association of strain with pathological features were assessed with Fisher's Exact test using JMP, Version 15 or 16 (SAS Institute). Quantitative immunoblotting and qRT-PCR data were analyzed by one-way ANOVA and Student's t-test, respectively, using Prism (GraphPad). Genotype-phenotype association in epistasis crosses were analyzed by linear regression modeling. Heterozygous and homozygous genotypes were independently coded to assess allelic dominance in both main and interaction effects. Significance was estimated by the ratio of F-statistics between interactive and additive models, with p-values derived from the Fisher-Snedecor distribution. ERG results were analyzed in Prism using a mixed effect model to accommodate missing data and to allow the use of repeated measures; further analysis of normalized data at the highest ERG flash intensities was performed in Prism using two-way ANOVA. A significance threshold of $p < 0.05$ was used for all experiments.

Supporting information

S1 Fig. Genome-wide recombination mapping of the *Tvrm323* mutation from 103 back-cross progeny ((*Tvrm323* × B6N) F$_1$ × B6N). Each column indicates a SNP and is ordered based on chromosome position. Homozygosity of the B6N allele is shown in yellow. The critical interval of the disease gene lies in the region highlighted in red, where ≥70% of the affected progeny were heterozygous for the corresponding SNP.
(TIF)

S2 Fig. Identification of causative mutations. A. Candidate-gene sequencing of the *Arhgef12* gene in B6 and affected *Tvrm266* mice identified a mutation in both heterozygous and homozygous individuals (yellow highlight). The mutation corresponds to c.71T>A. B. Candidate-gene sequencing of the *Prkci* gene in B6 and affected *Tvrm323* mice identified a mutation in both heterozygous and homozygous individuals (yellow highlight). The sequencing chromatograms shown correspond to the antisense strand. The mutation corresponds to c.406T>A. C. Co-segregation analysis of the disease phenotype with the *Arhgef12* mutation in a small mapping cross of *Tvrm266* mice with B6N mice. D. Co-segregation analysis of the disease phenotype with the *Prkci* mutation in the *Tvrm323* mapping cross.
(TIF)

S3 Fig. Western analysis of ARHGEF12 in posterior eyecup lysates. Equal amounts (20 μg) of B6, B6 *rd8*, and *Tvrm266* lysates prepared at one month of age were electrophoresed, transferred to nitrocellulose membranes and probed with antibodies against ARHGEF12 and GAPDH. Ponceau S staining was also performed to demonstrate equivalent loading of total protein.
(TIF)

S4 Fig. Quantitative western analysis of B6 and *Tvrm266* or *Tvrm323* eyecups collected from mice at approximately two months of age. Eyecups were lysed in electrophoresis sample buffer. The volumes loaded for electrophoresis are indicated by the values (in μl) above the blot images. The molecular weights of protein standards are indicated. A–E. ARHGEF12 quantitation. A. ARHGEF12 western blot. B. GAPDH western blot. C. Integrated intensities from lanes shown in panel A. Intensity was measured within a subregion of each lane corresponding to the migration of ARHGEF12 and plotted against sample load volume. Intensities

for the B6 standard curve are shown as black squares; the intensities for all 10 μl samples positioned along a hyperbolic fit to the standard curve are shown as red circles. D. Plot of integrated intensity and GAPDH bands from panel B. E. Relative ARHGEF12 levels and statistical analysis. Bars show mean ± SD. F–J. PRKCI quantitation. The blot images and corresponding analyses are identical to those in A–E, except antibody against PRKCI was used in panel F.
(TIF)

S5 Fig. Test of ELM fragmentation dependence on the homozygous *Crb1^{rd8}* allele. Ocular sections from mice at 10–16 weeks of age (n = 4 for both strains) were stained with DAPI to detect nuclei (blue) and TJP1 to detect the ELM (red). A. *Tvrm266* mice at 10 weeks of age. Gaps are indicated with yellow arrows. B. Mice bearing a homozygous *Arhgef12^{Tvrm266}* allele and a heterozygous *Crb1^{rd8}* allele were obtained from epistasis matings, 10 weeks of age. No gaps were observed. C. Quantitation of gaps per mm of ELM. Bars indicate mean ± SEM.
(TIF)

S1 Data. Data and statistical analysis to support the text, figures, and supporting information. Worksheet tabs correspond to individual data elements. Each worksheet includes the values used for plotting individual points and for computing cohort means and standard deviation or standard error of the mean. The corresponding statistical analysis is also included in each worksheet.
(XLSX)

Acknowledgments

Author Contributions

Conceptualization: Jürgen K. Naggert, Patsy M. Nishina.

Formal analysis: Sonia M. Weatherly, Jeremy R. Charette, Gregory W. Carter, Mark P. Krebs.

Funding acquisition: Gregory W. Carter, Jürgen K. Naggert, Mark P. Krebs, Patsy M. Nishina.

Investigation: Sonia M. Weatherly, Gayle B. Collin, Jeremy R. Charette, Lisa Stone, Nattaya Damkham, Lillian F. Hyde, Wanda Hicks, Jürgen K. Naggert, Mark P. Krebs, Patsy M. Nishina.

Methodology: Gayle B. Collin, Mark P. Krebs, Patsy M. Nishina.

Project administration: Gayle B. Collin, Patsy M. Nishina.

Resources: Sonia M. Weatherly, Lisa Stone, Mark P. Krebs, Patsy M. Nishina.

Software: James G. Peterson, Mark P. Krebs.

Supervision: Patsy M. Nishina.

Visualization: Sonia M. Weatherly, Gayle B. Collin, Mark P. Krebs.

Writing – original draft: Sonia M. Weatherly.

Writing – review & editing: Gayle B. Collin, Gregory W. Carter, Jürgen K. Naggert, Mark P. Krebs, Patsy M. Nishina.

References

1. den Hollander AI, Davis J, van der Velde-Visser SD, Zonneveld MN, Pierrottet CO, Koenekoop RK, et al. CRB1 mutation spectrum in inherited retinal dystrophies. Hum Mutat. 2004; 24: 355–369. https://doi.org/10.1002/humu.20093 PMID: 15459956

2. Bujakowska K, Audo I, Mohand-Said S, Lancelot ME, Antonio A, Germain A, et al. CRB1 mutations in inherited retinal dystrophies. Hum Mutat. 2012); 33: 306–315. https://doi.org/10.1002/humu.21653 PMID: 22065545

3. Ehrenberg M, Pierce EA, Cox GF, Fulton AB. CRB1: one gene, many phenotypes. Semin Ophthalmol. 2013; 28: 397–405. https://doi.org/10.3109/08820538.2013.825277 PMID: 24138049

4. Slavotinek AM. The Family of Crumbs Genes and Human Disease. Mol Syndromol. 2016; 7: 274–281. https://doi.org/10.1159/000448109 PMID: 27867342

5. Quinn PM PL, Wijnholds J. The CRB1 Complex: Following the Trail of Crumbs to a Feasible Gene Therapy Strategy. Front Neurosci. 2017; 11. https://doi.org/10.3389/fnins.2017.00175 PMID: 28424578

6. Ray TA, Cochran KJ, Kay JN. The Enigma of CRB1 and CRB1 Retinopathies. Adv Exp Med Biol. 2019; 1185: 251–255. https://doi.org/10.1007/978-3-030-27378-1_41 PMID: 31884620

7. Talib M, Boon CJF. Retinal Dystrophies and the Road to Treatment: Clinical Requirements and Considerations. Asia Pac J Ophthalmol (Phila). 2020; 9: 159–179. https://doi.org/10.1097/APO.0000000000000290 PMID: 32511120

8. den Hollander AI, ten Brink JB, de Kok YJ, van Soest S, van den Born LI, van Driel MA, et al. Mutations in a human homologue of Drosophila crumbs cause retinitis pigmentosa (RP12). Nat Genet. 1999; 23: 217–221. https://doi.org/10.1038/13848 PMID: 10508521

9. Tepass U, Theres C, Knust E. crumbs encodes an EGF-like protein expressed on apical membranes of Drosophila epithelial cells and required for organization of epithelia. Cell. 1990; 61: 787–799. https://doi.org/10.1016/0092-8674(90)90189-I PMID: 2344615

10. Bulgakova NA, Knust E. The Crumbs complex: from epithelial-cell polarity to retinal degeneration. J Cell Sci. 2009; 122: 2587–2596. https://doi.org/10.1242/jcs.023648 PMID: 19625503

11. Tepass U. The apical polarity protein network in Drosophila epithelial cells: regulation of polarity, junctions, morphogenesis, cell growth, and survival. Annu Rev Cell Dev Biol. 2012; 28: 655–685. https://doi.org/10.1146/annurev-cellbio-092910-154033 PMID: 22881460

12. Thompson BJ, Pichaud F, Roper K. Sticking together the Crumbs—an unexpected function for an old friend. Nat Rev Mol Cell Biol. 2013; 14: 307–314. https://doi.org/10.1038/nrm3568 PMID: 23609509

13. Pichaud F. PAR-Complex and Crumbs Function During Photoreceptor Morphogenesis and Retinal Degeneration. Front Cell Neurosci. 2018; 12: 90. https://doi.org/10.3389/fncel.2018.00090 PMID: 29651238

14. Chang B, Svoboda KKH, Liu X. Cell polarization: From epithelial cells to odontoblasts. Eur J Cell Biol. 2019; 98: 1–11. https://doi.org/10.1016/j.ejcb.2018.11.003 PMID: 30473389

15. Grawe F, Wodarz A, Lee B, Knust E, Skaer H. The Drosophila genes crumbs and stardust are involved in the biogenesis of adherens junctions. Development. 1996; 122: 951–959. https://doi.org/10.1242/dev.122.3.951 PMID: 8631272

16. Pellikka M, Tanentzapf G, Pinto M, Smith C, McGlade CJ, Ready DF, et al. Crumbs, the Drosophila homologue of human CRB1/RP12, is essential for photoreceptor morphogenesis. Nature. 2002; 416: 143–149. https://doi.org/10.1038/nature721 PMID: 11850625

17. Izaddoost S, Nam SC, Bhat MA, Bellen HJ, Choi KW. Drosophila Crumbs is a positional cue in photoreceptor adherens junctions and rhabdomeres. Nature. 2002; 416: 178–183. https://doi.org/10.1038/nature720 PMID: 11850624

18. Kraut RS, Knust E. Changes in endolysosomal organization define a pre-degenerative state in the crumbs mutant Drosophila retina. PLoS One. 2019; 14: e0220220. https://doi.org/10.1371/journal.pone.0220220 PMID: 31834921

19. Mehalow AK, Kameya S, Smith RS, Hawes NL, Denegre JM, Young JA, et al. CRB1 is essential for external limiting membrane integrity and photoreceptor morphogenesis in the mammalian retina. Hum Mol Genet. 2003; 12: 2179–2189. https://doi.org/10.1093/hmg/ddg232 PMID: 12915475

20. van de Pavert SA, Kantardzhieva A, Malysheva A, Meuleman J, Versteeg I, Levelt C, et al. Crumbs homologue 1 is required for maintenance of photoreceptor cell polarization and adhesion during light exposure. J Cell Sci. 2004; 117: 4169–4177. https://doi.org/10.1242/jcs.01301 PMID: 15316081

21. Ray TA, Cochran K, Kozlowski C, Wang J, Alexander G, Cady MA, et al. Comprehensive identification of mRNA isoforms reveals the diversity of neural cell-surface molecules with roles in retinal

development and disease. Nat Commun. 2020; 11: 3328. https://doi.org/10.1038/s41467-020-17009-7 PMID: 32620864

22. van de Pavert SA, Meuleman J, Malysheva A, Aartsen WM, Versteeg I, Tonagel F, et al. A single amino acid substitution (Cys249Trp) in Crb1 causes retinal degeneration and deregulates expression of pituitary tumor transforming gene Pttg1. J Neurosci. 2007; 27: 564–573. https://doi.org/10.1523/JNEUROSCI.3496-06.2007 PMID: 17234588

23. Aleman TS, Cideciyan AV, Aguirre GK, Huang WC, Mullins CL, Roman AJ, et al. Human CRB1-associated retinal degeneration: comparison with the rd8 Crb1-mutant mouse model. Invest Ophthalmol Vis Sci. 2011; 52: 6898–6910. https://doi.org/10.1167/iovs.11-7701 PMID: 21757580

24. Motta FL, Salles MV, Costa KA, Filippelli-Silva R, Martin RP, Sallum JMF. The correlation between CRB1 variants and the clinical severity of Brazilian patients with different inherited retinal dystrophy phenotypes. Sci Rep. 2017; 7: 8654. https://doi.org/10.1038/s41598-017-09035-1 PMID: 28819299

25. Talib M, van Schooneveld MJ, van Genderen MM, Wijnholds J, Florijn RJ, Ten Brink JB, et al. Genotypic and Phenotypic Characteristics of CRB1-Associated Retinal Dystrophies: A Long-Term Follow-up Study. Ophthalmology. 2017; 124: 884–895. https://doi.org/10.1016/j.ophtha.2017.01.047 PMID: 28341475

26. Pellikka M, Tepass U. Unique cell biological profiles of retinal disease-causing missense mutations in the polarity protein Crumbs. J Cell Sci. 2017; 130: 2147–2158. https://doi.org/10.1242/jcs.197178 PMID: 28515229

27. Gosens I, den Hollander AI, Cremers FP, Roepman R. Composition and function of the Crumbs protein complex in the mammalian retina. Exp Eye Res. 2008; 86: 713–726. https://doi.org/10.1016/j.exer.2008.02.005 PMID: 18407265

28. Saberi M, Golchehre Z, Karamzade A, Entezam M, Eshaghkhani Y, Alavinejad E, et al. CRB1-Related Leber Congenital Amaurosis: Reporting Novel Pathogenic Variants and a Brief Review on Mutations Spectrum. Iran Biomed J. 2019; 23: 362–368. https://doi.org/10.29252/.23.5.362 PMID: 31103025

29. Ahmed Khan S, Richard Nestel A. CRB1 Gene Mutation Causing Different Phenotypes of Leber Congenital Amaurosis in Siblings. J Ophthalmic Vis Res. 2019; 14: 518–524. https://doi.org/10.18502/jovr.v14i4.5467 PMID: 31875109

30. Yzer S, Fishman GA, Racine J, Al-Zuhaibi S, Chakor H, Dorfman A, et al. CRB1 heterozygotes with regional retinal dysfunction: implications for genetic testing of Leber congenital amaurosis. Invest Ophthalmol Vis Sci. 2006; 47: 3736–3744. https://doi.org/10.1167/iovs.05-1637 PMID: 16936081

31. Buchovecky CM, Turley SD, Brown HM, Kyle SM, McDonald JG, Liu B, et al. A suppressor screen in Mecp2 mutant mice implicates cholesterol metabolism in Rett syndrome. Nat Genet. 2013; 45: 1013–1020. https://doi.org/10.1038/ng.2714 PMID: 23892605

32. Ramsbottom SA, Thelwall PE, Wood KM, Clowry GJ, Devlin LA, Silbermann F, et al. Mouse genetics reveals Barttin as a genetic modifier of Joubert syndrome. Proc Natl Acad Sci U S A. 2020; 117: 1113–1118. https://doi.org/10.1073/pnas.1912602117 PMID: 31879347

33. Meyer KJ, Anderson MG. Genetic modifiers as relevant biological variables of eye disorders. Hum Mol Genet. 2017; 26: R58–R67. https://doi.org/10.1093/hmg/ddx180 PMID: 28482014

34. Chang B, Hawes NL, Hurd RE, Davisson MT, Nusinowitz S, Heckenlively JR. Retinal degeneration mutants in the mouse. Vision Res. 2002; 42: 517–525. https://doi.org/10.1016/s0042-6989(01)00146-8 PMID: 11853768

35. Luhmann UF, Carvalho LS, Holthaus SM, Cowing JA, Greenaway S, Chu CJ, et al. The severity of retinal pathology in homozygous Crb1rd8/rd8 mice is dependent on additional genetic factors. Hum Mol Genet. 2015; 24: 128–141. https://doi.org/10.1093/hmg/ddu424 PMID: 25147295

36. Mattapallil MJ, Wawrousek EF, Chan CC, Zhao H, Roychoudhury J, Ferguson TA, et al. The Rd8 mutation of the Crb1 gene is present in vendor lines of C57BL/6N mice and embryonic stem cells, and confounds ocular induced mutant phenotypes. Invest Ophthalmol Vis Sci. 2012; 53: 2921–2927. https://doi.org/10.1167/iovs.12-9662 PMID: 22447858

37. Chang B, Hurd RE, Wang J, Nishina PM. Survey of common eye diseases in laboratory mouse strains. Invest Ophthalmol Vis Sci. 2013; 54: 4974–4981. https://doi.org/10.1167/iovs.13-12289 PMID: 23800770

38. Luhmann UF, Lange CA, Robbie S, Munro PM, Cowing JA, Armer HE, et al. Differential modulation of retinal degeneration by Ccl2 and Cx3cr1 chemokine signalling. PLoS One. 2012; 7: e35551. https://doi.org/10.1371/journal.pone.0035551 PMID: 22545116

39. Markand S, Saul A, Tawfik A, Cui X, Rozen R, Smith SB. Mthfr as a modifier of the retinal phenotype of Crb1(rd8/rd8) mice. Exp Eye Res. 2016; 145: 164–172. https://doi.org/10.1016/j.exer.2015.11.013 PMID: 26646559

40. Kwon YS, Tham A, Lopez AJ, Edwards S, Woods S, Chen J, et al. Cytoglobin deficiency potentiates Crb1-mediated retinal degeneration in rd8 mice. Dev Biol. 2020; 458: 141–152. https://doi.org/10.1016/j.ydbio.2019.10.013 PMID: 31634437

41. Chang B, FitzMaurice B, Wang JP, Low BE, Wiles MV, Nishina PM. Spontaneous Posterior Segment Vascular Disease Phenotype of a Mouse Model, rnv3, Is Dependent on the Crb1(rd8) Allele. Invest Ophthalmol Vis Sci. 2018; 59: 5127–5139. https://doi.org/10.1167/iovs.18-25046 PMID: 30372741

42. Pellissier LP, Lundvig DM, Tanimoto N, Klooster J, Vos RM, Richard F, et al. CRB2 acts as a modifying factor of CRB1-related retinal dystrophies in mice. Hum Mol Genet. 2014; 23: 3759–3771. https://doi.org/10.1093/hmg/ddu089 PMID: 24565864

43. Quinn PM, Mulder AA, Henrique Alves C, Desrosiers M, de Vries SI, Klooster J, et al. Loss of CRB2 in Muller glial cells modifies a CRB1-associated retinitis pigmentosa phenotype into a Leber congenital amaurosis phenotype. Hum Mol Genet. 2019; 28: 105–123. https://doi.org/10.1093/hmg/ddy337 PMID: 30239717

44. Zhao Z, Chen Y, Wang J, Sternberg P, Freeman ML, Grossniklaus HE, et al. Age-related retinopathy in NRF2-deficient mice. PLoS One. 2011; 6: e19456. https://doi.org/10.1371/journal.pone.0019456 PMID: 21559389

45. Richert E, Klettner A, von der Burchard C, Roider J, Tode J. CRB1(rd8) mutation influences the age-related macular degeneration phenotype of NRF2 knockout mice and favors choroidal neovascularization. Adv Med Sci. 2020; 65: 71–77. https://doi.org/10.1016/j.advms.2019.11.003 PMID: 31918066

46. Won J, Shi LY, Hicks W, Wang J, Hurd R, Naggert JK, et al. Mouse model resources for vision research. J Ophthalmol. 2011; 2011: 391384. https://doi.org/10.1155/2011/391384 PMID: 21052544

47. Won J, Shi LY, Hicks W, Wang J, Naggert JK, Nishina PM. Translational vision research models program. Adv Exp Med Biol. 2012; 723: 391–397. https://doi.org/10.1007/978-1-4614-0631-0_50 PMID: 22183357

48. Krebs MP, Collin GB, Hicks WL, Yu M, Charette JR, Shi LY, et al. Mouse models of human ocular disease for translational research. PLoS One. 2017; 12: e0183837. https://doi.org/10.1371/journal.pone.0183837 PMID: 28859131

49. Nunes de Almeida F, Walther RF, Presse MT, Vlassaks E, Pichaud F. Cdc42 defines apical identity and regulates epithelial morphogenesis by promoting apical recruitment of Par6-aPKC and Crumbs. Development. 2019; 146: dev175497. https://doi.org/10.1242/dev.175497 PMID: 31405903

50. Bateson W. Mendel's Principles of Heredity. Cambridge, U.K.: Cambridge University Press; 1909.

51. Zhao M, Andrieu-Soler C, Kowalczuk L, Paz Cortes M, Berdugo M, Dernigoghossian M, et al. A new CRB1 rat mutation links Muller glial cells to retinal telangiectasia. J Neurosci. 2015; 35: 6093–6106. https://doi.org/10.1523/JNEUROSCI.3412-14.2015 PMID: 25878282

52. Pellissier LP, Alves CH, Quinn PM, Vos RM, Tanimoto N, Lundvig DM, et al. Targeted ablation of CRB1 and CRB2 in retinal progenitor cells mimics Leber congenital amaurosis. PLoS Genet. 2013; 9: e1003976. https://doi.org/10.1371/journal.pgen.1003976 PMID: 24339791

53. Margolis B, Borg JP. Apicobasal polarity complexes. J Cell Sci. 2005; 118: 5157–5159. https://doi.org/10.1242/jcs.02597 PMID: 16280548

54. Assemat E, Bazellieres E, Pallesi-Pocachard E, Le Bivic A, Massey-Harroche D. Polarity complex proteins. Biochim Biophys Acta. 2008; 1778: 614–630. https://doi.org/10.1016/j.bbamem.2007.08.029 PMID: 18005931

55. Campanale JP, Sun TY, Montell DJ. Development and dynamics of cell polarity at a glance. J Cell Sci. 2017; 130: 1201–1207. https://doi.org/10.1242/jcs.188599 PMID: 28365593

56. Rusu AD, Georgiou M. The multifarious regulation of the apical junctional complex. Open Biol. 2020; 10: 190278. https://doi.org/10.1098/rsob.190278 PMID: 32070233

57. Mack NA, Georgiou M. The interdependence of the Rho GTPases and apicobasal cell polarity. Small GTPases. 2014; 5: 10. https://doi.org/10.4161/21541248.2014.973768 PMID: 25469537

58. Citi S, Guerrera D, Spadaro D, Shah J. Epithelial junctions and Rho family GTPases: the zonular signalosome. Small GTPases. 2014; 5: 1–15. https://doi.org/10.4161/21541248.2014.973760 PMID: 25483301

59. Arnold TR, Stephenson RE, Miller AL. Rho GTPases and actomyosin: Partners in regulating epithelial cell-cell junction structure and function. Exp Cell Res. 2017; 358: 20–30. https://doi.org/10.1016/j.yexcr.2017.03.053 PMID: 28363828

60. Bloor JW, Kiehart DP. Drosophila RhoA regulates the cytoskeleton and cell-cell adhesion in the developing epidermis. Development. 2002; 129: 3173–3183. https://doi.org/10.1242/dev.129.13.3173 PMID: 12070092

61. Jensen AM, Walker C, Westerfield M. mosaic eyes: a zebrafish gene required in pigmented epithelium for apical localization of retinal cell division and lamination. Development. 2001; 128: 95–105. https://doi.org/10.1242/dev.128.1.95 PMID: 11092815

62. Hsu YC, Willoughby JJ, Christensen AK, Jensen AM. Mosaic Eyes is a novel component of the Crumbs complex and negatively regulates photoreceptor apical size. Development. 2006; 133: 4849–4859. https://doi.org/10.1242/dev.02685 PMID: 17092952

63. Wei X, Malicki J. nagie oko, encoding a MAGUK-family protein, is essential for cellular patterning of the retina. Nat Genet. 2002; 31: 150–157. https://doi.org/10.1038/ng883 PMID: 11992120

64. Omori Y, Malicki J. oko meduzy and related crumbs genes are determinants of apical cell features in the vertebrate embryo. Curr Biol. 2006; 16: 945–957. https://doi.org/10.1016/j.cub.2006.03.058 PMID: 16713951

65. Alves CH, Sanz Sanz A, Park B, Pellissier LP, Tanimoto N, Beck SC, et al. Loss of CRB2 in the mouse retina mimics human retinitis pigmentosa due to mutations in the CRB1 gene. Hum Mol Genet. 2013; 22: 35–50. https://doi.org/10.1093/hmg/dds398 PMID: 23001562

66. Alves CH, Bossers K, Vos RM, Essing AH, Swagemakers S, van der Spek PJ, et al. Microarray and Morphological Analysis of Early Postnatal CRB2 Mutant Retinas on a Pure C57BL/6J Genetic Background. PLoS One. 2013; 8: e82532. https://doi.org/10.1371/journal.pone.0082532 PMID: 24324803

67. Cho SH, Nahar A, Kim JH, Lee M, Kozmik Z, Kim S. Targeted deletion of Crb1/Crb2 in the optic vesicle models key features of leber congenital amaurosis 8. Dev Biol. 2019; 453: 141–154. https://doi.org/10.1016/j.ydbio.2019.05.008 PMID: 31145883

68. Cho SH, Kim JY, Simons DL, Song JY, Le JH, Swindell EC, et al. Genetic ablation of Pals1 in retinal progenitor cells models the retinal pathology of Leber congenital amaurosis. Hum Mol Genet. 2012; 21: 2663–2676. https://doi.org/10.1093/hmg/dds091 PMID: 22398208

69. Koike C, Nishida A, Akimoto K, Nakaya MA, Noda T, Ohno S, et al. Function of atypical protein kinase C lambda in differentiating photoreceptors is required for proper lamination of mouse retina. J Neurosci. 2005; 25: 10290–10298. https://doi.org/10.1523/JNEUROSCI.3657-05.2005 PMID: 16267237

70. Soloff RS, Katayama C, Lin MY, Feramisco JR, Hedrick SM. Targeted deletion of protein kinase C lambda reveals a distribution of functions between the two atypical protein kinase C isoforms. J Immunol. 2004; 173: 3250–3260. https://doi.org/10.4049/jimmunol.173.5.3250 PMID: 15322187

71. Lopez-Garcia LA, Schulze JO, Frohner W, Zhang H, Suss E, Weber N, et al. Allosteric regulation of protein kinase PKCzeta by the N-terminal C1 domain and small compounds to the PIF-pocket. Chem Biol. 2011; 18: 1463–1473. https://doi.org/10.1016/j.chembiol.2011.08.010 PMID: 22118680

72. Velnati S, Centonze S, Girivetto F, Capello D, Biondi RM, Bertoni A, et al. Identification of Key Phospholipids That Bind and Activate Atypical PKCs. Biomedicines. 2021; 9: 45. https://doi.org/10.3390/biomedicines9010045 PMID: 33419210

73. Roberts RK, Appel B. Apical polarity protein PrkCi is necessary for maintenance of spinal cord precursors in zebrafish. Dev Dyn. 2009; 238: 1638–1648. https://doi.org/10.1002/dvdy.21970 PMID: 19449304

74. Zheng Y. Dbl family guanine nucleotide exchange factors. Trends Biochem Sci. 2001; 26: 724–732. https://doi.org/10.1016/s0968-0004(01)01973-9 PMID: 11738596

75. Mosaddeghzadeh N, Ahmadian MR. The RHO Family GTPases: Mechanisms of Regulation and Signaling. Cells. 2021; 10: 1831. https://doi.org/10.3390/cells10071831 PMID: 34359999

76. Jaiswal M, Dvorsky R, Ahmadian MR. Deciphering the molecular and functional basis of Dbl family proteins: a novel systematic approach toward classification of selective activation of the Rho family proteins. J Biol Chem. 2013; 288: 4486–4500. https://doi.org/10.1074/jbc.M112.429746 PMID: 23255595

77. Reuther GW, Lambert QT, Booden MA, Wennerberg K, Becknell B, Marcucci G, et al. Leukemia-associated Rho guanine nucleotide exchange factor, a Dbl family protein found mutated in leukemia, causes transformation by activation of RhoA. J Biol Chem. 2001; 276: 27145–27151. https://doi.org/10.1074/jbc.M103565200 PMID: 11373293

78. Booden MA, Siderovski DP, Der CJ. Leukemia-associated Rho guanine nucleotide exchange factor promotes G alpha q-coupled activation of RhoA. Mol Cell Biol. 2002; 22: 4053–4061. https://doi.org/10.1128/MCB.22.12.4053-4061.2002 PMID: 12024019

79. Muller PM, Rademacher J, Bagshaw RD, Wortmann C, Barth C, van Unen J, et al. Systems analysis of RhoGEF and RhoGAP regulatory proteins reveals spatially organized RAC1 signalling from integrin adhesions. Nat Cell Biol. 2020; 22: 498–511. https://doi.org/10.1038/s41556-020-0488-x PMID: 32203420

80. Guo Z, Neilson LJ, Zhong H, Murray PS, Zanivan S, Zaidel-Bar R. E-cadherin interactome complexity and robustness resolved by quantitative proteomics. Sci Signal. 2014; 7: rs7. https://doi.org/10.1126/scisignal.2005473 PMID: 25468996

81. Kim JH, Mukherjee A, Madhavan SM, Konieczkowski M, Sedor JR. WT1-interacting protein (Wtip) regulates podocyte phenotype by cell-cell and cell-matrix contact reorganization. Am J Physiol Renal Physiol. 2012; 302: F103–115. https://doi.org/10.1152/ajprenal.00419.2011 PMID: 21900451

82. Ninomiya K, Ohta K, Yamashita K, Mizuno K, Ohashi K. PLEKHG4B enables actin cytoskeletal remodeling during epithelial cell-cell junction formation. J Cell Sci. 2021; 134: jcs249078. https://doi.org/10.1242/jcs.249078 PMID: 33310911

83. Chikumi H, Vazquez-Prado J, Servitja JM, Miyazaki H, Gutkind JS. Potent activation of RhoA by Galpha q and Gq-coupled receptors. J Biol Chem. 2002; 277: 27130–27134. https://doi.org/10.1074/jbc.M204715200 PMID: 12016230

84. Suzuki N, Nakamura S, Mano H, Kozasa T. Galpha 12 activates Rho GTPase through tyrosine-phosphorylated leukemia-associated RhoGEF. Proc Natl Acad Sci U S A. 2003; 100: 733–738. https://doi.org/10.1073/pnas.0234057100 PMID: 12515866

85. Pfreimer M, Vatter P, Langer T, Wieland T, Gierschik P, Moepps B. LARG links histamine-H1-receptor-activated Gq to Rho-GTPase-dependent signaling pathways. Cell Signal. 2012; 24: 652–663. https://doi.org/10.1016/j.cellsig.2011.10.014 PMID: 22100544

86. Siehler S. Regulation of RhoGEF proteins by G12/13-coupled receptors. Br J Pharmacol. 2009; 158: 41–49. https://doi.org/10.1111/j.1476-5381.2009.00121.x PMID: 19226283

87. Suzuki N, Hajicek N, Kozasa T. Regulation and physiological functions of G12/13-mediated signaling pathways. Neurosignals. 2009; 17: 55–70. https://doi.org/10.1159/000186690 PMID: 19212140

88. van Rossum AG, Aartsen WM, Meuleman J, Klooster J, Malysheva A, Versteeg I, et al. Pals1/Mpp5 is required for correct localization of Crb1 at the subapical region in polarized Müller glia cells. Hum Mol Genet. 2006; 15: 2659–2672. https://doi.org/10.1093/hmg/ddl194 PMID: 16885194

89. den Hollander AI, Ghiani M, de Kok YJ, Wijnholds J, Ballabio A, Cremers FP, et al. Isolation of Crb1, a mouse homologue of Drosophila crumbs, and analysis of its expression pattern in eye and brain. Mech Dev. 2002; 110: 203–207. https://doi.org/10.1016/s0925-4773(01)00568-8 PMID: 11744384

90. Smith TL, Oubaha M, Cagnone G, Boscher C, Kim JS, El Bakkouri Y, et al. eNOS controls angiogenic sprouting and retinal neovascularization through the regulation of endothelial cell polarity. Cell Mol Life Sci. 2021; 79: 37. https://doi.org/10.1007/s00018-021-04042-y PMID: 34971428

91. Riddell M, Nakayama A, Hikita T, Mirzapourshafiyi F, Kawamura T, Pasha A, et al. aPKC controls endothelial growth by modulating c-Myc via FoxO1 DNA-binding ability. Nat Commun. 2018; 9: 5357. https://doi.org/10.1038/s41467-018-07739-0 PMID: 30559384

92. Kusuhara S, Fukushima Y, Fukuhara S, Jakt LM, Okada M, Shimizu Y, et al. Arhgef15 promotes retinal angiogenesis by mediating VEGF-induced Cdc42 activation and potentiating RhoJ inactivation in endothelial cells. PLoS One. 2012; 7: e45858. https://doi.org/10.1371/journal.pone.0045858 PMID: 23029280

93. Balasubramanian R, Min X, Quinn PMJ, Giudice QL, Tao C, Polanco K, et al. Phase transition specified by a binary code patterns the vertebrate eye cup. Sci Adv. 2021; 7: eabj9846. https://doi.org/10.1126/sciadv.abj9846 PMID: 34757798

94. Macosko EZ, Basu A, Satija R, Nemesh J, Shekhar K, Goldman M, et al. Highly Parallel Genome-wide Expression Profiling of Individual Cells Using Nanoliter Droplets. Cell. 2015; 161: 1202–1214. https://doi.org/10.1016/j.cell.2015.05.002 PMID: 26000488

95. Joly S, Pernet V, Samardzija M, Grimm C. Pax6-positive Muller glia cells express cell cycle markers but do not proliferate after photoreceptor injury in the mouse retina. Glia. 2011; 59: 1033–1046. https://doi.org/10.1002/glia.21174 PMID: 21500284

96. Lewis GP, Chapin EA, Luna G, Linberg KA, Fisher SK. The fate of Muller's glia following experimental retinal detachment: nuclear migration, cell division, and subretinal glial scar formation. Mol Vis. 2010; 16: 1361–1372. PMID: 20664798

97. Paun CC, Pijl BJ, Siemiatkowska AM, Collin RW, Cremers FP, Hoyng CB, et al. A novel crumbs homolog 1 mutation in a family with retinitis pigmentosa, nanophthalmos, and optic disc drusen. Mol Vis. 2012; 18: 2447–2453. PMID: 23077403

98. Wolfson Y, Applegate CD, Strauss RW, Han IC, Scholl HP. CRB1-Related Maculopathy With Cystoid Macular Edema. JAMA Ophthalmol. 2015; 133: 1357–1360. https://doi.org/10.1001/jamaophthalmol.2015.2814 PMID: 26312378

99. Talib M, Van Cauwenbergh C, De Zaeytijd J, Van Wynsberghe D, De Baere E, Boon CJF, et al. CRB1-associated retinal dystrophies in a Belgian cohort: genetic characteristics and long-term clinical follow-up. Br J Ophthalmol. 2021; 106: 696–704. https://doi.org/10.1136/bjophthalmol-2020-316781 PMID: 33579689

100. Shen W, Fruttiger M, Zhu L, Chung SH, Barnett NL, Kirk JK, et al. Conditional Muller cell ablation causes independent neuronal and vascular pathologies in a novel transgenic model. J Neurosci. 2012; 32: 15715–15727. https://doi.org/10.1523/JNEUROSCI.2841-12.2012 PMID: 23136411

101. Pawelec P, Ziemka-Nalecz M, Sypecka J, Zalewska T. The Impact of the CX3CL1/CX3CR1 Axis in Neurological Disorders. Cells. 2020; 9: 2277. https://doi.org/10.3390/cells9102277 PMID: 33065974

102. Fodinger M, Horl WH, Sunder-Plassmann G. Molecular biology of 5,10-methylenetetrahydrofolate reductase. J Nephrol. 2000; 13: 20–33. PMID: 10720211

103. Thuy le TT, Van Thuy TT, Matsumoto Y, Hai H, Ikura Y, Yoshizato K, et al. Absence of cytoglobin promotes multiple organ abnormalities in aged mice. Sci Rep. 2016; 6: 24990. https://doi.org/10.1038/srep24990 PMID: 27146058

104. Musso T, Johnston JA, Linnekin D, Varesio L, Rowe TK, O'Shea JJ, et al. Regulation of JAK3 expression in human monocytes: phosphorylation in response to interleukins 2, 4, and 7. J Exp Med. 1995; 181: 1425–1431. https://doi.org/10.1084/jem.181.4.1425 PMID: 7535338

105. Kawamura M, McVicar DW, Johnston JA, Blake TB, Chen YQ, Lal BK, et al. Molecular cloning of L-JAK, a Janus family protein-tyrosine kinase expressed in natural killer cells and activated leukocytes. Proc Natl Acad Sci U S A. 1994; 91: 6374–6378. https://doi.org/10.1073/pnas.91.14.6374 PMID: 8022790

106. Vomund S, Schafer A, Parnham MJ, Brune B, von Knethen A. Nrf2, the Master Regulator of Anti-Oxidative Responses. Int J Mol Sci. 2017; 18. https://doi.org/10.3390/ijms18122772 PMID: 29261130

107. Austin CP, Battey JF, Bradley A, Bucan M, Capecchi M, Collins FS, et al. The knockout mouse project. Nat Genet. 2004; 36: 921–924. https://doi.org/10.1038/ng0904-921 PMID: 15340423

108. Birling MC, Yoshiki A, Adams DJ, Ayabe S, Beaudet AL, Bottomley J, et al. A resource of targeted mutant mouse lines for 5,061 genes. Nat Genet. 2021; 53: 416–419. https://doi.org/10.1038/s41588-021-00825-y PMID: 33833456

109. Soewarto D, Klaften M, Rubio-Aliaga I. Features and strategies of ENU mouse mutagenesis. Curr Pharm Biotechnol. 2009; 10: 198–213. https://doi.org/10.2174/138920109787315079 PMID: 19199953

110. Tomberg K, Westrick RJ, Kotnik EN, Cleuren AC, Siemieniak DR, Zhu G, et al. Whole exome sequencing of ENU-induced thrombosis modifier mutations in the mouse. PLoS Genet. 2018; 14: e1007658. https://doi.org/10.1371/journal.pgen.1007658 PMID: 30188893

111. Schindelin J, Arganda-Carreras I, Frise E, Kaynig V, Longair M, Pietzsch T, et al. Fiji: an open-source platform for biological-image analysis. Nat Methods. 2012; 9: 676–682. https://doi.org/10.1038/nmeth.2019 PMID: 22743772

112. Krebs MP, Xiao M, Sheppard K, Hicks W, Nishina PM. Bright-field imaging and optical coherence tomography of the mouse posterior eye. Methods Mol Biol. 2016; 1438: 395–415. https://doi.org/10.1007/978-1-4939-3661-8_20 PMID: 27150100

113. Fairfield H, Gilbert GJ, Barter M, Corrigan RR, Curtain M, Ding Y, et al. Mutation discovery in mice by whole exome sequencing. Genome Biol. 2011; 12: R86. https://doi.org/10.1186/gb-2011-12-9-r86 PMID: 21917142

114. Krebs MP. Using Vascular Landmarks to Orient 3D Optical Coherence Tomography Images of the Mouse Eye. Curr Protoc Mouse Biol. 2017; 7: 176–190. https://doi.org/10.1002/cpmo.32 PMID: 28884793

115. Collin GB, Won J, Krebs MP, Hicks WJ, Charette JR, Naggert JK, et al. Disruption in murine Eml1 perturbs retinal lamination during early development. Sci Rep. 2020; 10: 5647. https://doi.org/10.1038/s41598-020-62373-5 PMID: 32221352

116. Kinoshita J, Peachey NS. Noninvasive Electroretinographic Procedures for the Study of the Mouse Retina. Curr Protoc Mouse Biol. 2018; 8: 1–16. https://doi.org/10.1002/cpmo.39 PMID: 30040236